A β-barrel for oil transport through lipid membranes: Dynamic NMR structures of AlkL

Tobias Schubeis, Tanguy Le Marchand, Csaba Daday, Wojciech Kopec, Kumar Tekwani Movellan, Jan Stanek, Tom S Schwarzer, Kathrin Castiglione, Bert L de Groot, Guido Pintacuda, et al.

A β-barrel for oil transport through lipid membranes: Dynamic NMR structures of AlkL

Tobias Schubeis[a], Tanguy Le Marchand[a], Csaba Daday[b], Wojciech Kopec[b], Kumar Tekwani Movellan[c], Jan Stanek[a,1], Tom S. Schwarzer[d], Kathrin Castiglione[d,2], Bert L. de Groot[b], Guido Pintacuda[a,3], and Loren B. Andreas[a,c,3]

[a]Centre de Résonance Magnétique Nucléaire à Très Hauts Champs de Lyon (FRE 2034–CNRS, Université Claude Bernard Lyon 1, École Normale Supérieure Lyon), Université de Lyon, 69100 Villeurbanne, France; [b]Biomolecular Dynamics Group, Max Planck Institute for Biophysical Chemistry, 37077 Göttingen, Germany; [c]Department for NMR-based Structural Biology, Max Planck Institute for Biophysical Chemistry, 37077 Göttingen, Germany; and [d]Institute of Biochemical Engineering, Technical University of Munich, 85748 Garching, Germany

Edited by David Baker, University of Washington, Seattle, WA, and approved July 22, 2020 (received for review February 14, 2020)

The protein AlkL is known to increase permeability of the outer membrane of bacteria for hydrophobic molecules, yet the mechanism of transport has not been determined. Differing crystal and NMR structures of homologous proteins resulted in a controversy regarding the degree of structure and the role of long extracellular loops. Here we solve this controversy by determining the de novo NMR structure in near-native lipid bilayers, and by accessing structural dynamics relevant to hydrophobic substrate permeation through molecular-dynamics simulations and by characteristic NMR relaxation parameters. Dynamic lateral exit sites large enough to accommodate substrates such as carvone or octane occur through restructuring of a barrel extension formed by the extracellular loops.

membrane protein | lipid bilayers | protein structure | protein dynamics | magic-angle spinning

As in any cell, the outer membrane of bacteria is composed of a lipid bilayer that separates intracellular processes from the outside environment. In addition to this lipid bilayer, Gram-negative bacteria have evolved an outer leaflet composed mainly of lipopolysaccharides (LPS) (1). While the inner membrane is permeable to hydrophobic molecules, the charged and densely packed LPS layer reduces their permeation rates 50–100-fold, as compared with phospholipid membranes (2–4) (Fig. 1). Since these membrane properties limit uptake of nutrients, bacteria make use of a wide array of passive transmembrane porins, β-barrels of sufficiently large diameter to allow nonspecific permeation of small molecules (1, 5).

The OmpW family of outer-membrane proteins (6), classified as porins, is widespread in Gram-negative bacteria. These proteins fold into eight-stranded β-barrels displaying a narrow pore diameter in the membrane, which appears too compact to permit passage of even small molecular substrates. Yet there is mounting evidence that the OmpW family protein AlkL functions as a passive importer of hydrophobic molecules. AlkL is found on the same operon together with genes necessary for oxidation of alkanes and utilization as a carbon and energy source (7) (Fig. 1). These include an alkane monooxygenase (AlkB) and associated rubredoxin (AlkG) and rubredoxin reductase (AlkT), as well as an aldehyde dehydrogenase (AlkH) and alcohol dehydrogenase (AlkK) and a positive regulatory protein (AlkS). Due to its location on the *alk* operon, AlkL was proposed to have a passive transport function, increasing the rate of diffusion for alkanes. Definitive evidence for such transport was recently found by incorporating the alkane hydroxylase complex of *Pseudomonas putida GPo1* with and without AlkL in cells (8–10), and in even more defined nanoreactor polymersomes (11). These studies demonstrate transport of alkanes, and a cyclic methyl ketone, respectively, in line with the wide substrate utilization of *P. putida*. In polymersomes, the increase in transport-dependent production of product alcohol occurs with an increase in the number of incorporated AlkL molecules.

While the transport function of AlkL has been established, a controversy in the transport mechanism still exists. By analogy to other β-barrels (12–15), a lateral exit was proposed based on X-ray structures of OmpW (16) and OprG (17), formed from proline residues that break the hydrogen bonding at the end of the transmembrane β-strands. The X-ray structure reveals a β-barrel arrangement in the loops; however, the 1.3-Å radius of the putative lateral opening is incompatible with the size of known substrates of AlkL such as alkanes or monocyclic molecules. The static X-ray structures are therefore insufficient to explain the mode of action, and a view complemented by dynamics is needed (18–20). In contrast, micellar solution NMR structures lack the putative exit sites entirely, and rather display flexible extracellular loops (21, 22). This supports an alternative vision of transport characterized by hinge motions of the loops and major rearrangements of backbone segments or partial loss of secondary structure. Here we solve this controversy by determining the de novo NMR structure in near-native lipid bilayers for AlkL, and by detecting structural dynamics relevant to

Significance

Here we show how AlkL, a minimalistic outer-membrane protein from oil-consuming bacteria, exploits dynamics of extracellular loops to channel substrate across the polysaccharide barrier and into the hydrophobic interior of the outer membrane. This work represents a unique example of a side-by-side atomic-level structure determination by solution NMR in detergents and by solid-state NMR in lipid bilayers, which critically demonstrates the importance of a lipid environment to investigate function. Corroborating our experimental measurements, molecular-dynamics simulations capture substrate transit via lateral openings. The capacity to unravel membrane protein function under near-native conditions, fueled by the latest method developments, opens up a new frontier for their investigation, and provides thereby for improved fundamental insights into biological processes.

Author contributions: T.S., B.L.d.G., G.P., and L.B.A. designed research; T.S., T.L.M., C.D., W.K., K.T.M., J.S., and L.B.A. performed research; T.S.S. and K.C. contributed new reagents/analytic tools; T.S., T.L.M., C.D., W.K., K.T.M., J.S., and L.B.A. analyzed data; and T.S., B.L.d.G., G.P., and L.B.A. wrote the paper.

The authors declare no competing interest.

This article is a PNAS Direct Submission.

[1]Present address: Faculty of Chemistry, University of Warsaw, 02089 Warsaw, Poland.

[2]Present address: Chemical and Biological Engineering, Institute of Bioprocess Engineering, Friedrich-Alexander-Universität Erlangen-Nürnberg, 91052 Erlangen, Germany.

[3]To whom correspondence may be addressed. Email: Guido.Pintacuda@ens-lyon.fr or land@nmr.mpibpc.mpg.de.

This article contains supporting information online at https://www.pnas.org/lookup/suppl/doi:10.1073/pnas.2002598117/-/DCSupplemental.

First published August 19, 2020.

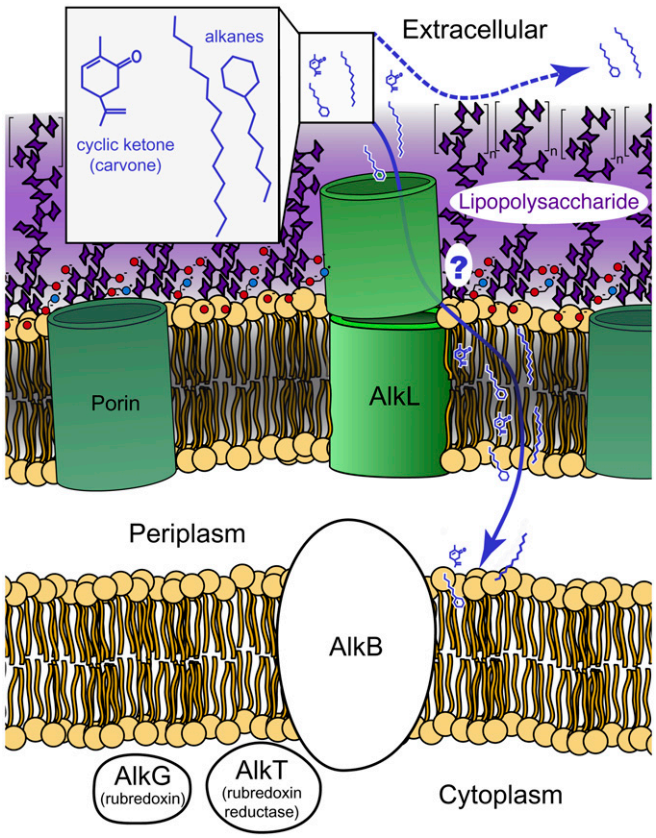

Fig. 1. The main features of the inner and outer membranes of Gram-negative bacteria, and location of key proteins of the Alk operon. Hydrophobic molecules such as alkanes and terpenoids (*Inset*, blue), do not readily traverse (blue dashed arrow) the LPS (purple). Instead, their permeation is assisted by porins such as AlkL (green). A permeation path through the extracellular loops with a lateral exit into the hydrophobic bilayer (blue arrow) was proposed based on crystal structures of AlkL homologs (8). Detergent micelle solution data support a more dynamic process without a specific lateral release (21, 22).

hydrophobic substrate permeation through molecular-dynamics (MD) simulations and by characteristic NMR relaxation parameters. The data revealed a dynamic lateral exit mechanism that involves continuous restructuring of the barrel extension and release into the lipid bilayer through ephemeral openings.

Results and Discussion

To understand the mechanism of the transport function of AlkL, we determined two separate structures, one in detergent micelles by using well-established solution NMR protocols and a second in lipid bilayers, by using the latest magic-angle spinning (MAS) NMR methodology. This is complemented by characterization of structural dynamics by both simulation and NMR relaxation measurements. The solution NMR data were acquired from octyl glucoside solution (OG), with traces of the refolding detergent LDAO using a perdeuterated AlkL sample. Both of these detergents are considered mild. Lipid-embedded AlkL data were acquired from 1,2-dimyristoyl-*sn*-glycero-3-phosphocholine (DMPC) bilayer samples, as well as from preparations reconstituted in the presence of LPS, using both fully protonated as well as perdeuterated AlkL. In these latter preparations, negative stain transmission electron micrographs reveal the presence of liposomes, without detectable protein aggregates (*SI Appendix*, Fig. S1). Furthermore, NMR experiments probing protein-to-lipid interactions demonstrate that AlkL is in immediate contact with lipids (23). Residues all across the β-barrel show contact with the lipid acyl chains, defining the transmembrane region of the protein (*SI Appendix*, Fig. S2). For sensitivity reasons, the lipid-to-protein ratio (LPR) was minimized to 0.5 by mass (~18 by mole). The resulting spectrum at LPR of 0.5 is unchanged from an LPR of 10, but spectral quality degrades with LPR of 0.25 (*SI Appendix*, Fig. S3). This combined evidence shows that AlkL is properly embedded in the membrane and that the protein structure is independent of concentration over the range detectable by MAS NMR.

NMR Structures. Two structures were determined from assigned resonances in 170 out of 203 residues in lipids, and 132 residues in detergent. Unassigned signals in lipids belong mainly to the flexible *N*- terminus, to periplasmic turns, and to short portions of the first extracellular loop, and are absent from many of the NMR spectra. In detergent, only the first loop was assigned, and displays chemical shifts characteristic of unstructured proteins. Approximatively 50 additional unassigned signals in the 2D ^{1}H-^{15}N heteronuclear single quantum coherence fall in the same chemical shift range, indicating a lack of β-structure also for the remaining loops. This is in contrast to the DMPC preparation where assignments in all loops indicate structure. No nuclear Overhauser effect (NOE) transfer to these peaks was observed, also pointing to lack of structure. Yet additional evidence pointing toward random coiled loops in detergents was obtained by preparing a sample in D_2O. In D_2O only the assigned residues of the transmembrane region remained detectable, indicating protection from HD exchange. In an MSP1 nanodisc preparation (*SI Appendix*, Fig. S4) without detergent, mainly unassigned residues appeared, indicating that the rigid transmembrane domain is not detectable in the larger nanodisc particle. Consistent with the DMPC preparation where more loop residues are structured, some peaks that were flexible in detergent are not detected in the nanodisc preparation.

Structures were calculated from a clear pattern of proton–proton cross-strand contacts in radio-frequency–driven recoupling (RFDR) or NOE spectra. While traditional three-dimensional (3D) HHN- and HNN NOE spectroscopy (NOESY) spectra provided sufficient resolution in solution, we turned to four-dimensional (4D) HNNH-RFDR spectra in solids to remove ambiguities in the assignment of cross-strand restraints (*SI Appendix*, Figs. S5 and S6). The fully protonated sample together with >100-kHz MAS (24) granted access to sidechain resonance assignments and collection of sidechain-to-sidechain distance restraints which was used to refine the bilayer-bound structure. All restraints used for calculation of the two structures are listed in *SI Appendix*, Table S2.

The two AlkL structures determined by MAS and solution NMR are shown in Fig. 2 *A* and *B*, and share an identical transmembrane (TM) β-barrel motif. The lipid-embedded structure, however, reveals an elongated β-barrel fold, extending into the region where polysaccharide would be in LPS, similar to homologous crystal structures. Structured loop residues also occur in a sample reconstituted in the presence of LPS and DMPC lipids (*SI Appendix*, Fig. S7) as indicated by the detection of the same loop resonances in cross-polarization–based spectra. Only minor chemical shift perturbation (CSP) is observed. Conversely, the loops are highly flexible in OG detergent micelles, which is in turn consistent with previous determinations of homologs by solution NMR. That the bilayer-embedded structure in this case appears closer to homology models of crystal structures is in contrast to a recent solid-state NMR structure of OmpG (25) obtained in 2D crystalline lipid bilayers, which agreed better with the solution NMR conformation. In the case of AlkL, the perturbation due to

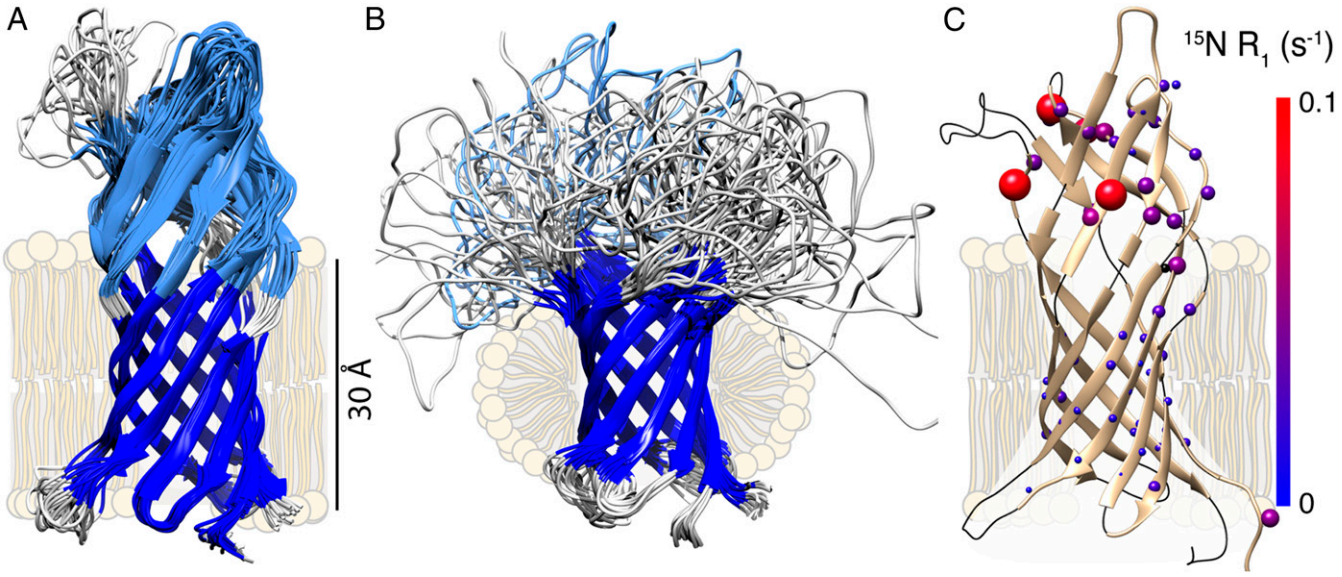

Fig. 2. NMR structure and dynamics of AlkL. The structural ensembles in lipids and in detergent are depicted in *A* and *B*, respectively. Loops (that form a barrel extension in *A*) are colored in light blue where residues are assigned, and in gray where no assignment could be made. Temperatures were 305 K for the lipid bilayer sample and 308 K for the detergent-solubilized sample. In *C*, ^{15}N R_1 rates in lipids are indicated on the lowest-energy conformer of the protein structure in *A*.

detergent micelles appears to outweigh the influence of crystal contacts.

Site-specific ^{15}N longitudinal relaxation (R_1) (26) in the lipid-embedded sample explains the apparent inconsistency between the two models in lipids and in micelles, by assessing dynamic motions occurring on a fast (nanosecond) timescale (Fig. 2*C* and *SI Appendix*, Table S3). While the TM region displays uniform low relaxation rates, the extracellular portion is subject to enhanced *ns* backbone dynamics. These measurements define a clear junction in flexibility between the TM and extracellular regions of the structure. Considering that transport through the AlkL inner pore would require channel opening, the low R_1 relaxation rates of the TM region are in favor of a model where the TM region is serving solely as an anchor for the more flexible extracellular part. This complements the rigid representation of extracellular β-strands in Fig. 2*A*, and is consistent with the fact that a detergent environment (Fig. 2*B*) results in loss of structure in the loops. The same mobility that is likely needed to allow for the transport function of the protein appears to predispose the extracellular part to destabilization by even mild detergent, an effect which likely plagues other membrane proteins (27).

Since the lipid bilayer most closely mimics the native membrane, and these conditions support a folded extracellular domain, we focused on the membrane-embedded sample and solid-state NMR for further structural and dynamical analysis of transport in AlkL. The surface hydrophobicity of the bilayer NMR structure (Fig. 3*A*) demonstrates the expected hydrophobic exterior (tan) in the transmembrane region, with polar and charged residues lining the interior. Reverse polarity (purple) is seen on the extracellular barrel extension, which has a hydrophilic exterior.

These structural features define a long, accessible hydrophobic pore, leading up to the membrane interfacial region. Within the TM domain, the pore narrows to less than the radius of a water molecule as visualized using HOLE (28) (Fig. 3*B*), which along with a hydrophilic character suggests lateral release into the hydrophobic membrane rather than continued transport through the protein. A cross-sectional view (Fig. 3*D*) reveals the tight stacking of long internal sidechains that block diffusion of molecules through the TM region. At the same time, the structure features six small openings, two of which (I and IV) are located close to the membrane surface (Fig. 3*C*), in the vicinity of several proline residues that break the pattern of cross-strand hydrogen bonds. Site I is the most prominent in our NMR structure, while site IV corresponds to the previously proposed putative lateral exit (8, 16, 17). These potential exit sites would require dynamic rearrangement to accommodate the size of substrate. Detailed views of the hydrophobic residues lining the extracellular pore are displayed in Fig. 3 *D* and *E*. The residue R168 is shown occluding the pore at the top of the TM barrel, and in the same view, the residues V75 and T54 are seen near the mouth of the largest potential exit site I/II.

Dynamical Lateral Release Model. The validity of this "dynamical lateral release" model is supported by MD simulations (Figs. 4 and 5) and NMR relaxation rates sensitive to slow motions (Fig. 6), recorded both in the presence and the absence of the substrates octane and carvone. *P. putida* utilizes a wide substrate range including linear alkanes, cyclic hydrocarbons, and even polycyclic molecules (PAHs) (7). The alkanes are metabolized by the alk proteins, whereas PAHs are utilized by additional metabolic pathways, making octane an ideal molecule to investigate the transport function of AlkL. All simulations were initiated in explicit water from the solid-state NMR structure of AlkL embedded in a membrane. Simulations in LPS membrane (details in the *SI Appendix*) were initiated with 1-palmitoyl-2-oleoyl-*sn*-glycero-3-phosphocholine on the inner leaflet (Fig. 4). These MD simulations conform to the expected behavior of the LPS, namely, that the hydrophobic octane does not traverse the barrier characterized by polar sugar moieties functionalized with charged phosphate groups. As expected, octane enters the hydrophobic pore formed by loop residues, and traverses this region of the protein up until the level of the lipid head groups. At this point, the pore is occluded by charged sidechains, in particular R168. Fig. 4 *A* and *B* shows two snapshots from the MD

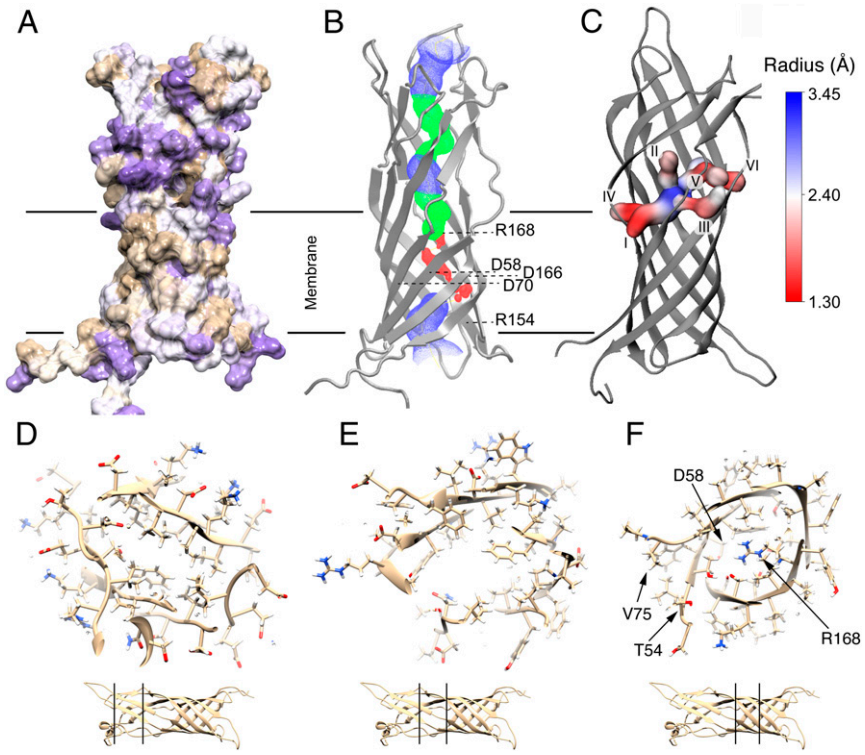

Fig. 3. The bilayer structure of AlkL, and potential exit. *A* shows surface hydrophobicity (tan) and hydrophilicity (purple). In *B*, the central pore is visualized using the HOLE (*18*) program. Red indicates a diameter less than one water molecule (1.15 Å), while green and blue indicate a radius of one water (1.15–2.30 Å), and more than one water molecule (>2.30 Å), respectively. The positions of charged residues constraining the interior are labeled. In *C*, potential lateral exit sites are visualized. In *D–F*, slices through the β-barrel extension are characterized by a hydrophobic inner surface (*D* and *E*), with the central pore blocked by arginine in the membrane-embedded part of the protein *F*. In the same vicinity, a lateral opening occurs near residues T54 and V75.

trajectory, as well as a comparison of the bilayer penetration depth of octane in LPS alone and mediated by AlkL (Fig. 4*A*, *Inset*). This comparison was made with the zero depth referenced to the LPS phosphate groups. Consistent with the low rate (millisecond timescale) of transport that supports growth of yeast and *E. coli* on sugar (29–31), these 1 μs MD trajectories were not able to capture substrate permeation events, even when reinitialized from structures where octane was already bound in the pore. Nonetheless, the protein did readily allow deep penetration of substrate into the membrane, and we were able to observe full octane transit in MD trajectories in a simplified DMPC environment. Fig. 4 *C–E* shows several snapshots from 1-μs trajectories in which octane escaped into the lipid membrane from three different interstrand locations, namely sites I and IV identified in Fig. 3*C* as well as between P147 and P171. While the LPS appears to stabilize the protein, increasing the energy barrier for such events, the events may nevertheless represent permeation pathways albeit that occur much more slowly in the native membrane.

In addition to octane, we observed permeation for the monocyclic ketone carvone, which is an intermediate-sized oil that provides a challenging test of the transport function of AlkL. Carvone has a similar structure to a cyclic methyl ketone used to demonstrate accelerated transport facilitated by AlkL (11). Fig. 5*A* shows the initial conformation of AlkL embedded into a DMPC membrane in explicit water. The simulations in DMPC match the conditions of the NMR structure determination, where the protein was properly folded. Over multiple microsecond trajectories, the structure is stable, and the barrel extension exhibits higher plasticity than the transmembrane region, in agreement with the experimental data. Within 100 ns, carvone molecules cluster onto the barrel extension and several molecules are seen to concurrently occupy the pore (Fig. 5*B*). After 1,000 ns, all carvone molecules have diffused into the membrane or remain within the barrel extension (Fig. 5*C*). Although this simulation time was again not sufficient to observe lateral release of carvone, release did occur in further simulations, initialized from structures where carvone was already bound in the pore (see *SI Appendix*, Figs. S8 and S9 for the detailed simulation protocols). As visualized by four snapshots in Fig. 5*D*, carvone is observed to exit toward the membrane uniquely through site I. This shows that exit of both octane, and the larger carvone molecule is possible without a pair of proline residues breaking cross-strand hydrogen bonds, and therefore represents a distinct class of lateral exit site. The simulations in DMPC do not preserve the barrier properties of LPS. They can therefore not be used to assess AlkL-mediated acceleration of permeation, but can be used to probe the permeation pathway. As expected, most carvone molecules enter the membrane directly in DMPC, and relatively few carvone molecules enter the membrane via AlkL. This nevertheless demonstrates the transport function of the protein. Since there is no active transport in AlkL, we expect nearly all octane or carvone to partition to the hydrophobic membrane, and this is indeed observed in long enough MD simulations. In a living system, consumption of the substrate occurs via AlkB in the inner membrane, necessitating exit from the inner leaflet of the outer membrane, and entry into the inner membrane lipids. To our knowledge, these phospholipid membranes do not present a substantial barrier to AlkB substrates, and no additional proteins have been identified in the passive flux of metabolites once through the LPS barrier.

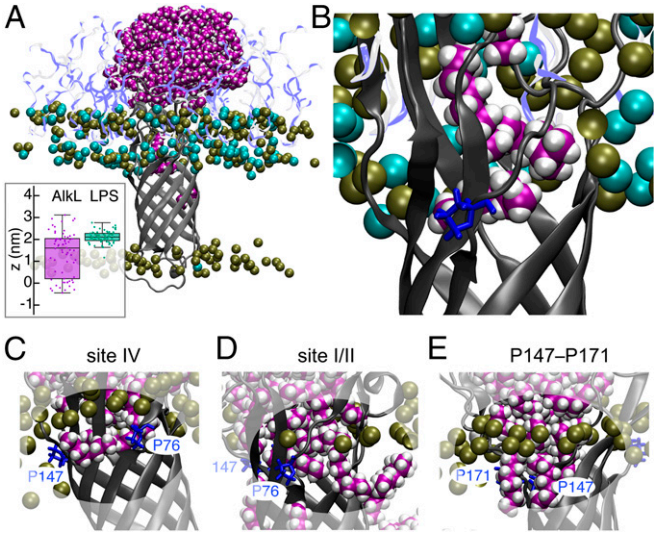

Fig. 4. MD simulations of AlkL in LPS (*A* and *B*) and in DMPC (*C*–*E*) with the substrate octane. Octane enters the protein and reaches near the depth (z) of the acyl lipid chains (*A*, *Inset*). A "prerelease" snapshot of octane in LPS is shown in *B*. Three different octane release locations were observed in DMPC lipids, at the site IV proposed in homologs (*C*), through the new site I/II (*D*), and through the prolines P147 and 171 (*E*), on the opposite side of the barrel. LPS sugars are displayed in purple, phosphate in dark green, calcium in cyan, and the protein in gray. Octane is shown in purple and white spheres.

Transit events through AlkL are made possible by dynamic remodeling of the pore, as evidenced by the distinct distributions of conformers in the absence and presence of carvone (Fig. 5 *E* and *F*). Notably, the main conformers identified in simulations with bound carvone (Fig. 5*E*) mostly retained a widened potential exit site I, as compared to the NMR structure (Fig. 3*C*). Furthermore, there is hardly any overlap in the phase-space regions explored by the protein without and with bound carvone (Fig. 5*F*). Interestingly, the NMR structure is located in between these two regions. The motion along the first (largest) eigenvector in a principal component analysis (PCA) shows that the difference without and with bound carvone is related to the opening of the newly identified site I for carvone permeation (Movie S1).

We used two further NMR measurements to detect structural variations and motional processes relevant to hydrophobic substrate permeation: chemical shift perturbations (CSPs) and ^{15}N longitudinal relaxation under RF spin lock ($R_{1\rho}$) (Fig. 6 and *SI Appendix*, Table S3). High CSPs highlight significant changes in the barrel extension for both carvone and octane. Of particular interest are large CSP values in residues flanking P76, which lies in a β-bulge separating sites I and IV. Coincident with large CSPs are enhanced values of ^{15}N $R_{1\rho}$ (Fig. 6*C*), an indicator of transient chemical shift changes (exchange phenomena) and microsecond–millisecond motions. $R_{1\rho}$ rates were also sensitive to the presence of carvone in the barrel extension (*SI Appendix*, Fig. S10). Overall, the NMR data are direct signatures of the transient expansion of the pore captured by MD simulations, providing a connection between loop flexibility and permeation. Of the sites implicated by dynamics measurements, sites III–VI are flanked by β-strands with a well-defined hydrogen bonding pattern in lipids (*SI Appendix*, Fig. S11), indicating a more static structure. Only the site I/II is larger and adjacent to the highly flexible loop 1. It is no surprise that this location supports dynamic release of the larger carvone molecule.

Whether the dynamic lateral release mechanism described here is general for proteins of the OmpW family remains an open question. While for AlkL, there is no evidence for hydrophilic substrates, and indeed no CSP was observed in AlkL with leucine as substrate (*SI Appendix*, Fig. S12), amino acids have been proposed for homologous proteins. If an OmpW family protein does accommodate hydrophilic substrates, lateral transport may represent the first part of the mechanism, which would traverse the polysaccharide barrier of the outer membrane. Complete traversal would then require transmembrane passage through the aliphatic lipid tails, which presents a barrier to hydrophilic substrate. This might occur via oligomeric interfaces or partner proteins. For example, crystal packing interactions are found in OmpW crystals (Protein Data Bank [PDB] ID code 2F1V) in a region corresponding to the exit site in AlkL (*SI Appendix*, Fig. S11), and a pore large enough for glycine is found in a homology model of OprG based on the OmpW crystal structure (32). Alternatively, OmpW family members might act in concert with other proteins present in the outer membrane in a similar way as a type 9 secretion system that exports protein through a lateral exit to a porin (33). Although no such protein has been identified, the outer membrane is rich with a plethora of membrane proteins that may play a role. Further evidence is needed to understand whether AlkL homologs exhibit the same transport function via a lateral release mechanism as proposed here for AlkL.

Conclusions. Through a combination of NMR and MD simulations, we uncovered a dynamic translocation pathway in an eight-stranded β-barrel for the import of hydrophobic molecules. The side-by-side comparison of sample conditions shows a strong impact of lipids and LPS in particular in stabilizing the protein. This demonstrates that even a β-barrel, often regarded as particularly stable, can be strongly impacted by environmental conditions in the functionally important extracellular loops. The sensitivity to environmental conditions also explains discrepancies related to environmental influences affecting crystal and solution structures. The capacity of NMR to site-specifically probe structure and dynamics of membrane proteins in lipid bilayers was the foundation for these mechanistic insights, and is key to understanding proteins in motion. Here specifically, the transmembrane transport mechanism that is implicated by CSP and MD provides the underpinning for potential future biotechnology and bioengineering applications.

Methods

Sample Preparation. Uniformly ^{13}C,^{15}*N*-labeled and ^{2}H,^{13}C,^{15}*N*-labeled samples of AlkL (28-230) from *P. putida* GPo1 were expressed in *Escherichia coli*, purified, and reconstituted in lipids according to a protocol described previously (34), and recently adapted to accommodate isotopic labeling (35). A full description is provided in *SI Appendix*, *Supplementary Text*. Samples in the presence of octane or carvone were prepared in saturated solutions, by addition of a small drop of oil to the surface of the sample buffer. Liposomes were separated by centrifugation before packing in NMR rotors.

NMR Spectroscopy. Solution NMR spectra were recorded at $\omega_{0H}/2\pi$ = 1 GHz and 600 MHz on Bruker Avance III instruments equipped with cryogenic probes using ^{2}H,^{13}C,^{15}*N*-labeled AlkL. Solid-state NMR spectra were recorded at $\omega_{0H}/2\pi$ = 1 GHz and 800 MHz, on Bruker Avance III instruments equipped with 0.7- and 1.3-mm HCN probes spinning at MAS rates of 111.111 kHz (^{13}C,^{15}*N*-labeled AlkL) or 60 kHz (^{2}H,^{13}C,^{15}*N*-labeled AlkL). Spectrometer settings, as well as acquisition parameters specific for each 3D and 4D spectrum, and for site-specific ^{15}N R_1 (26) and ($R_{1\rho}$) (36) rates, are discussed in *SI Appendix*, *Supplementary Text* and summarized in *SI Appendix*, Table S1. The spectral quality underlying resonance assignment datasets (37, 38) is demonstrated in the pair of CA-*N*-H correlation spectra shown in *SI Appendix*, Fig. S13 and the assignments are discussed in detail in a separate manuscript (39). CSPs induced by the presence of carvone or octane were

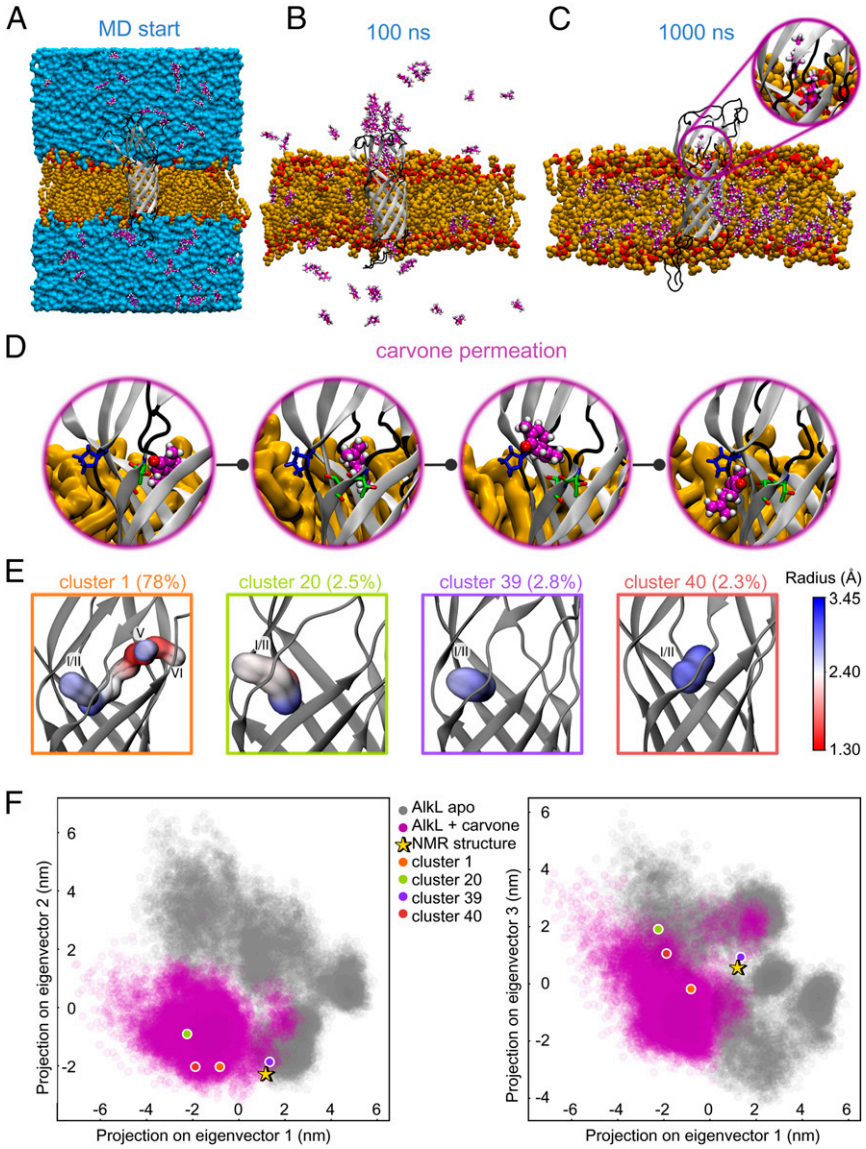

Fig. 5. MD simulations of AlkL in DMPC with and without carvone. *A–C* show simulation snapshots in which carvone molecules (magenta) spontaneously enter both the membrane (orange) and the protein (gray) from explicit water (blue). *D* shows a full permeation event, in which one carvone molecule exits the protein through site I/II and emerges near the lipid headgroup. Lining the exit, threonine residues 53, 54 and proline 76 are shown as green and blue sticks, respectively. *E* shows central structures of main clusters (occurrence % indicated) identified in MD simulations with bound carvone and the lateral exits in each cluster. *F* shows the projections of simulations into first three eigenvectors obtained through PCA of all MD trajectories.

obtained from (H)CANH and (H)CONH spectra, and were calculated as the RMSD of ^{1}H, ^{13}CA, and ^{15}N shifts, with relative scaling of 1, 0.3, and 0.15, respectively (40).

Solution NMR Structure Calculation. Several unambiguous distance restraints were manually assigned in the well-resolved 3D (H)N(HH)NH spectrum, leading, along with dihedral angle restraints, to an initial model. A set of hydrogen bond restraints was generated for resonances that showed no exchange with D_2O. NOESY peak lists were added for automated assignment and structure calculation using CYANA 3.98 (41). Further details are discussed in *SI Appendix, Supplementary Text*, and calculation statistics are reported in *SI Appendix*, Table S2.

MAS NMR Structure Calculation. Several unambiguous distance restraints were manually assigned in the well-resolved 4D (H)NH(H)NH spectrum leading, along with dihedral angle restraints, to a first model. Hydrogen bond restraints were included where cross-peaks in the 4D spectrum were identified with β-sheet chemical shift, and forming a clear pattern of contacts expected for antiparallel β-sheets (*SI Appendix*, Figs. S3 and S4). The hydrogen bond restrains are indicated in *SI Appendix*, Fig. S11. RFDR and band-selective spectral spin diffusion–SD (35) peak lists were added for automated assignment and structure calculation using CYANA 3.98 (41). The final structure made use of both backbone and sidechain protons (*SI Appendix*, Fig. S14). Further details are discussed in *SI Appendix, Supplementary Text*, and calculation statistics are reported in *SI Appendix*, Table S2.

Relaxation Data Fitting. Signal intensity decays of both ^{15}N R_1 and $R_{1\rho}$ relaxation experiments were fit to a monoexponential function. Error estimate was performed with Monte Carlo simulations: synthetic datasets are produced by adding Gaussian random noise (with the same SD as the experimental noise) to the backcalculated decay curves. The error was determined as the SD of the ensemble of dynamical parameters obtained by fitting 1,000 synthetic datasets.

MD Simulations. All simulations were performed with GROMACS 2018 simulation software (42). *SI Appendix, Supplementary Text* discusses the details

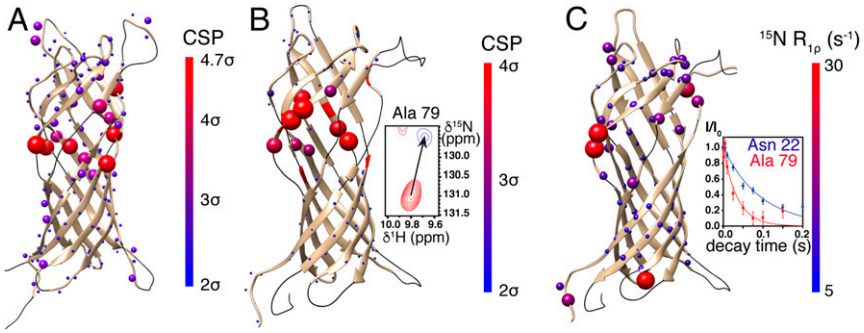

Fig. 6. Mapping the conduction pathway. *A* and *B* show CSP upon addition of the substrates octane and carvone, respectively. *B* (*Inset*) shows the amide ^{1}H-^{15}N correlation peak of Ala-79 before (red lines) and after addition of carvone (blue lines). *C* shows ^{15}N $R_{1\rho}$ relaxation rates, a measure of microsecond–millisecond motions. (*Inset*) Relaxation curves obtained for a rigid (Asn-22, blue) and a more flexible residue (Ala-79, red) are shown.

of the force fields and parameters used, as well as the procedures for preparing the systems prior to MD simulations. Four systems containing AlkL were simulated for 1,000 ns each ("Alk apo" simulations). After the addition of carvone, four new systems were initially simulated for 1,000 ns each. Further simulations were spawned by monitoring the position of bound carvone and simulated for additional 100 ns in several cycles, as shown in *SI Appendix*, Fig. S6.

Data Availability. The atomic coordinates and restraints were deposited in the Protein Data Bank, https://www.wwpdb.org/ [PDB ID codes 6QWR (43) and 6QAM (44)], and chemical shifts were deposited in the Biological Magnetic Resonance Data Bank, http://www.bmrb.wisc.edu/ [ID 34365 (45) and 34338 (46)].

ACKNOWLEDGMENTS. The work was funded by the European Research Council (ERC-2015-CoG GA 648974 to G.P.), the CNRS (IR-RMN FR3050), the European Commission (Project iNext GA 653706), the German Research Foundation (Emmy Noether Program Grant AN1316/1-1 and SFB803 Grant INST 186/794-3 Project B11 to L.B.A.; FOR 2518 "DynIon," Project P5 to W.K. and B.L.d.G.), and the German Federal Ministry of Education and Research (BMBF GA 031A178 to K.C.). J.S. was supported by MSCA incoming fellowship GA 661799.

1. R. Koebnik, K. P. Locher, P. Van Gelder, Structure and function of bacterial outer membrane proteins: Barrels in a nutshell. *Mol. Microbiol.* **37**, 239–253 (2000).
2. R. R. Chen, Permeability issues in whole-cell bioprocesses and cellular membrane engineering. *Appl. Microbiol. Biotechnol.* **74**, 730–738 (2007).
3. R. E. Hancock, The bacterial outer membrane as a drug barrier. *Trends Microbiol.* **5**, 37–42 (1997).
4. H. Nikaido, Prevention of drug access to bacterial targets: Permeability barriers and active efflux. *Science* **264**, 382–388 (1994).
5. H. Nikaido, Porins and specific channels of bacterial outer membranes. *Mol. Microbiol.* **6**, 435–442 (1992).
6. J. W. Fairman, N. Noinaj, S. K. Buchanan, The structural biology of β-barrel membrane proteins: A summary of recent reports. *Curr. Opin. Struct. Biol.* **21**, 523–531 (2011).
7. J. D. Van Hamme, A. Singh, O. P. Ward, Recent advances in petroleum microbiology. *Microbiol. Mol. Biol. Rev.* **67**, 503–549 (2003).
8. C. Grant *et al*., Identification and use of an alkane transporter plug-in for applications in biocatalysis and whole-cell biosensing of alkanes. *Sci. Rep.* **4**, 5844 (2014).
9. M. K. Julsing *et al*., Outer membrane protein AlkL boosts biocatalytic oxyfunctionalization of hydrophobic substrates in Escherichia coli. *Appl. Environ. Microbiol.* **78**, 5724–5733 (2012).
10. Y. M. van Nuland, G. Eggink, R. A. Weusthuis, Application of AlkBGT and AlkL from Pseudomonas putida GPo1 for selective alkyl ester ω-Oxyfunctionalization in Escherichia coli. *Appl. Environ. Microbiol.* **82**, 3801–3807 (2016).
11. T. S. Schwarzer, L. Klermund, G. Wang, K. Castiglione, Membrane functionalization of polymersomes: Alleviating mass transport limitations by integrating multiple selective membrane transporters for the diffusion of chemically diverse molecules. *Nanotechnology* **29**, 44LT01 (2018).
12. H. Dong *et al*., Structural basis for outer membrane lipopolysaccharide insertion. *Nature* **511**, 52–56 (2014).
13. E. M. Hearn, D. R. Patel, B. W. Lepore, M. Indic, B. van den Berg, Transmembrane passage of hydrophobic compounds through a protein channel wall. *Nature* **458**, 367–370 (2009).
14. S. Qiao, Q. Luo, Y. Zhao, X. C. Zhang, Y. Huang, Structural basis for lipopolysaccharide insertion in the bacterial outer membrane. *Nature* **511**, 108–111 (2014).
15. B. van den Berg, P. N. Black, W. M. Clemons Jr., T. A. Rapoport, Crystal structure of the long-chain fatty acid transporter FadL. *Science* **304**, 1506–1509 (2004).
16. H. Hong, D. R. Patel, L. K. Tamm, B. van den Berg, The outer membrane protein OmpW forms an eight-stranded beta-barrel with a hydrophobic channel. *J. Biol. Chem.* **281**, 7568–7577 (2006).
17. D. S. Touw, D. R. Patel, B. van den Berg, The crystal structure of OprG from Pseudomonas aeruginosa, a potential channel for transport of hydrophobic molecules across the outer membrane. *PLoS One* **5**, e15016 (2010).
18. K. Oxenoid, J. J. Chou, A functional NMR for membrane proteins: Dynamics, ligand binding, and allosteric modulation. *Protein Sci.* **25**, 959–973 (2016).
19. A. Sekhar, L. E. Kay, An NMR view of protein dynamics in health and disease. *Annu. Rev. Biophys.* **48**, 297–319 (2019).
20. K. Wüthrich, G. Wagner, Internal motion in globular proteins. *Trends Biochem. Sci.* **3**, 227–230 (1978).
21. R. Horst, P. Stanczak, K. Wüthrich, NMR polypeptide backbone conformation of the E. coli outer membrane protein W. *Structure* **22**, 1204–1209 (2014).
22. I. Kucharska, P. Seelheim, T. Edrington, B. Liang, L. K. Tamm, OprG harnesses the dynamics of its extracellular loops to transport small amino acids across the outer membrane of Pseudomonas aeruginosa. *Structure* **23**, 2234–2245 (2015).
23. E. E. Najbauer *et al*., Probing membrane protein insertion into lipid bilayers by solid-state NMR. *ChemPhysChem* **20**, 302–310 (2019).
24. L. B. Andreas *et al*., Structure of fully protonated proteins by proton-detected magic-angle spinning NMR. *Proc. Natl. Acad. Sci. U.S.A.* **113**, 9187–9192 (2016).
25. J. S. Retel *et al*., Structure of outer membrane protein G in lipid bilayers. *Nat. Commun.* **8**, 2073 (2017).
26. N. Giraud *et al*., Quantitative analysis of backbone dynamics in a crystalline protein from nitrogen-15 spin-lattice relaxation. *J. Am. Chem. Soc.* **127**, 18190–18201 (2005).
27. C. Chipot *et al*., Perturbations of native membrane protein structure in alkyl phosphocholine detergents: A critical assessment of NMR and biophysical studies. *Chem. Rev.* **118**, 3559–3607 (2018).
28. O. S. Smart, J. M. Goodfellow, B. A. Wallace, The pore dimensions of gramicidin A. *Biophys. J.* **65**, 2455–2460 (1993).
29. R. J. Naftalin, N. Green, P. Cunningham, Lactose permease H+-lactose symporter: Mechanical switch or Brownian ratchet? *Biophys. J.* **92**, 3474–3491 (2007).
30. E. B. Waygood, T. Steeves, Enzyme I of the phosphoenolpyruvate: Sugar phosphotransferase system of Escherichia coli. Purification to homogeneity and some properties. *Can. J. Biochem.* **58**, 40–48 (1980).
31. L. Ye, J. A. Berden, K. van Dam, A. L. Kruckeberg, Expression and activity of the Hxt7 high-affinity hexose transporter of Saccharomyces cerevisiae. *Yeast* **18**, 1257–1267 (2001).
32. R. R. Sanganna Gari *et al*., Quaternary structure of the small amino acid transporter OprG from *Pseudomonas aeruginosa*. *J. Biol. Chem.* **293**, 17267–17277 (2018).
33. F. Lauber, J. C. Deme, S. M. Lea, B. C. Berks, Type 9 secretion system structures reveal a new protein transport mechanism. *Nature* **564**, 77–82 (2018).
34. T. S. Schwarzer, M. Hermann, S. Krishnan, F. C. Simmel, K. Castiglione, Preparative refolding of small monomeric outer membrane proteins. *Protein Expr. Purif.* **132**, 171–181 (2017).
35. M. G. Jain *et al*., Selective ^{1}H-^{1}H distance restraints in fully protonated proteins by very fast magic-angle spinning solid-state NMR. *J. Phys. Chem. Lett.* **8**, 2399–2405 (2017).
36. J. R. Lewandowski, H. J. Sass, S. Grzesiek, M. Blackledge, L. Emsley, Site-specific measurement of slow motions in proteins. *J. Am. Chem. Soc.* **133**, 16762–16765 (2011).

37. E. Barbet-Massin *et al*., Rapid proton-detected NMR assignment for proteins with fast magic angle spinning. *J. Am. Chem. Soc.* **136**, 12489–12497 (2014).
38. J. Stanek *et al*., NMR spectroscopic assignment of backbone and side-chain protons in fully protonated proteins: Microcrystals, sedimented assemblies, and amyloid fibrils. *Angew. Chem. Int. Ed. Engl.* **55**, 15504–15509 (2016).
39. T. Schubeis *et al*., Resonance assignment of the outer membrane protein AlkL in lipid bilayers by proton-detected solid-state NMR. *Biomol. NMR Assign.*, 10.1007/s12104-020-09964-5 (2020).
40. E. A. Chekmenev, J. Paulino, R. Fu, T. A. Cross, "Anisotropic and isotropic chemical shifts perturbations from solid state NMR spectroscopy for structural and functional biology" in *Modern Magnetic Resonance*, G. A. Webb, Ed. (Springer International Publishing, Cham, 2018), pp. 505–519.
41. P. Güntert, L. Buchner, Combined automated NOE assignment and structure calculation with CYANA. *J. Biomol. NMR* **62**, 453–471 (2015).
42. D. Van Der Spoel *et al*., GROMACS: Fast, flexible, and free. *J. Comput. Chem.* **26**, 1701–1718 (2005).
43. T. Schubeis, L. B. Andreas, G. Pintacuda, Solid-state NMR structure of outer membrane protein AlkL in DMPC lipid bilayers. Protein Data Bank. https://www.rcsb.org/structure/6qwr. Deposited 6 March 2019.
44. T. Schubeis, L. B. Andreas, G. Pintacuda, Solution NMR structure of outer membrane protein AlkL. Protein Data Bank. https://www.rcsb.org/structure/6qam. Deposited 19 December 2018.
45. T. Schubeis, L. B. Andreas, G. Pintacuda, Solid-state NMR structure of outer membrane protein AlkL in DMPC lipid bilayers. Biological Magnetic Resonance Data Bank. http://www.bmrb.wisc.edu/data_library/summary/index.php?bmrbId=34365. Deposited 6 March 2019.
46. T. Schubeis, L. B. Andreas, G. Pintacuda, Solution NMR structure of outer membrane protein AlkL. Biological Magnetic Resonance Data Bank. http://www.bmrb.wisc.edu/data_library/summary/index.php?bmrbId=34338. Deposited 19 December 2018.

PNAS
www.pnas.org

Supplementary Information for

A beta-barrel for oil transport through lipid membranes: dynamic NMR structures of AlkL

Tobias Schubeis[1], Tanguy Le Marchand[1], Csaba Daday[2] Wojciech Kopec[2], Kumar Tekwani Movellan[3], Jan Stanek[1]†, Tom S. Schwarzer[4], Kathrin Castiglione[4]‡, Bert L. de Groot[2], Guido Pintacuda[1]* & Loren B. Andreas[1,3]*

Loren B. Andreas
land@nmr.mpibpc.mpg.de

Guido Pintacuda
guido.pintacuda@ens-lyon.fr

This PDF file includes:

Other supplementary materials for this manuscript include the following:

One Supplementary Movie

Supplementary Text

Methods

Sample preparation. AlkL (28-230) from *Pseudomonas putida* GPo1 (Uniprot Q00595) with a C-terminal His-8 tag was expressed in *E. coli* as inclusion bodies, purified under denaturing conditions and refolded into LDAO micelles. A detailed protocol for AlkL refolding has been described previously(1) and was recently adapted to accommodate isotopic labelling(2). Isotopic labelling was performed in minimal media containing 4 g/L ^{13}C-glucose and 1 g/L $^{15}NH_4Cl$ (U-CN protein) or 4 g/L ^{13}C,^{2}H-glucose and 1 g/L $^{15}NH_4Cl$ in D_2O (U-DCN protein, 100% back exchange of NH-protons during purification). The detergent was exchanged to 2% octyl glucoside (OG) using a PD10 desalting column for solution NMR as well as for reconstitution into Lipids. The final solution NMR sample contained 330 µM U-DCN AlkL in 2 % OG and NMR buffer composed of 20 mM Sodium Phosphate at pH 7, with 10 mM glutamate, 10 mM arginine, and 0.02 % sodium azide. Traces of the refolding detergent LDAO may remain. To identify residues involved in hydrogen bonds, the buffer was exchanged to 20 mM Sodium Phosphate pH 7, 95% D_2O using a desalting column. In order to allow solution NMR analysis of AlkL in lipids, a nanodisc sample was prepared according to published protocols using membrane scaffold protein (MSP1D1)(3).

Lipid bilayer samples for solid-state NMR were prepared by addition of DMPC (10 mg/ml, multilamellar vesicles in H_2O) to AlkL in OG detergent at a lipid to protein ratio of 1:2 (w/w). Protein and lipids form soluble mixed micelles at this stage. Detergent was subsequently removed by dialysis against NMR buffer resulting in formation of multilamellar vesicles that precipitate within 24 hours. The white precipitate was collected by centrifugation using a table top centrifuge, resuspended in 0.5 ml buffer and packed into 1.3 or 0.7 mm rotors (Bruker) using an ultracentrifuge packing device (Giotto Biotech). To investigate the effect of the presence of a hydrophobic small molecule, a solid-state NMR sample was equilibrated with buffer saturated with carvone or octane and compared with a second rotor packed from the same batch of precipitated protein.

The bilayer sample in LPS (Sigma, phenol extract purified from *E. Coli* K-235) were prepared in an identical manner, except that the reconstitution was performed from AlkL in OG detergent with a ratio of DMPC:LPS:AlkL of 1:1:2 (by weight). The pellet was nearly transparent, different from the white precipitate that forms in the presence of DMPC alone. The spectrum (Fig S5) is nearly unchanged as compared to the DMPC preparation.

Solution NMR Spectroscopy. Triple resonance solution NMR spectra were recorded on a 600 MHz Bruker Avance III instrument equipped with a cryogenic probe. TROSY based HSQC, HNCA, HN(CO)CA, HNCACB, HNCO, and HN(CA)CO spectra were used for resonance assignment(4). To obtain distance restraints, a 3D NOESY-^{15}N-TROSY (NHH) and a 3D ^{15}N-HSQC- NOESY-^{15}N-HSQC (NNH) was recorded on a 1000 MHz Bruker Avance III instrument equipped with a cryogenic probe. All spectra were recorded at a sample temperature of 308 K.

Solid state NMR Spectroscopy. NMR spectra for the assignment of backbone and sidechain resonances were (H)NH, (H)CH, (H)CANH, (H)(CO)CA(CO)NH, (H)CONH, (HCA)CB(CA)NH, (HCA)CB (CACO)NH, (H)NCAHA, (H)N(CO)CAHA, (H)CCH, (H)COCAHA, (H)CO(N)CAHA. These spectra were recorded on U-CN AlkL in a 0.7 mm MAS rotor at 111 kHz on a 1000 MHz Bruker Avance III spectrometer (5, 6). Additionally, we recorded spectra for assignments, (H)CANH, (HCO)CA(CO)NH, (H)CONH, (H)CO(CA)NH, (HCA)CB(CA)NH, on U-DCN AlkL in a 1.3 mm MAS rotor at 60 kHz on a 800 MHz Bruker Avance III spectrometer. To obtain distance restraints, we recorded H(H)NH and H(H)CH using RFDR, H(H)NH, (H)N(HH)NH and (H)C(HH)CH using BASS-SD on U-CN AlkL as well as a 4D (H)NH(H)NH using RFRD on U-DCN AlkL(2, 7). Further experimental details are tabulated in Extended Data Table 1. Relaxation rates (^{15}N R_1 and $R_{1\rho}$) were determined using a modified 3D (H)CONH experiment (pseudo-4D), with the longest relaxation delay at 54 seconds for R_1 and 200 ms for $R_{1\rho}$. Chemical shift perturbations induced by the presence of either octane or carvone were measured under saturating concentrations of the small molecule, and were evaluated as a combination of ^{1}H, ^{15}N and ^{13}CA shift changes, with relative scaling of 1, 0.15, and 0.3: $CSP = \sqrt{\frac{1}{3}(\partial\Delta_H{}^2 + 0.15\partial\Delta_N{}^2 + 0.3\partial\Delta_{CA}{}^2)}$. All spectra were recorded at a sample temperature of 305 ± 3 K.

Table S1. NMR parameters for RFDR and BASS-SD spectra.

Experiment	H(H)NH	H(H)NH	(H)N(HH)NH	H(H)CH	(H)C(HH)CH	(H)NH(H)NH	(H)NH(H)NH
Sample	$^{13}C,^{15}N$	$^{13}C,^{15}N$	$^{13}C,^{15}N$	$^{13}C,^{15}N$	$^{13}C,^{15}N$	$^{2}H,^{13}C,^{15}N$	$^{2}H,^{13}C,^{15}N$
Spectrometer (MHz)	1000	1000	1000	1000	1000	1000	800
MAS, ν_r (kHz)	111	111	111	111	111	60	60
Heteronuclear transfer 1	H-N CP	H-N CP	H-N CP	H-C CP	H-C CP	H-N CP	H-N CP
Field (kHz)	1.4/0.4 ν_r	1.4/0.4 ν_r	1.4/0.4 ν_r	1.4/0.4 ν_r	1.4/0.4 ν_r	1.6/0.6 ν_r	1.7/0.7ν_r
Time (ms)*	1	0.6	0.6	0.5	0.35	1	1
Heteronuclear transfer 2	N-H CP	N-H CP	N-H CP	C-H CP	C-H CP	N-H CP	N-H CP
Field (kHz)	0.4/1.4 ν_r	0.4/1.4 ν_r	0.4/1.4 ν_r	0.4/1.4 ν_r	0.4/1.4 ν_r	0.6/1.6 ν_r	0.7/1.7ν_r
Time (ms)*	0.4	0.3	0.3	200	0.19	0.6	0.6
H-H Transfer	RFDR	BASS-SD	BASS-SD	RFDR	BASS-SD	RFDR	RFDR
Field (kHz)	192	6.25	6.25	192	4.1	100	100
Time (ms)*	0.5	6	6	0.5	4.5	3	0.5
Heteronuclear transfer 3	–	–	H-N CP	–	H-C CP	H-N CP	H-N CP
Field (kHz)	–	–	1.4/0.4 ν_r	–	1.4/0.4 ν_r	1.6/0.6 ν_r	1.7/0.7ν_r
Time (ms)*	–	–	0.6	–	0.35	1	1
Heteronuclear transfer 4	–	–	N-H CP	–	C-H CP	N-H CP	N-H CP
Field (kHz)	–	–	0.4/1.4 ν_r	–	0.4/1.4 ν_r	0.6/1.6 ν_r	0.7/1.7ν_r
Time (ms)*	–	–	0.3	–	0.19	0.6	0.6
sw (t1) (ppm)	12.5	35	35	12.5	38	6.5	7
Acq.time (t1) (ms)	4.6	9	9	4.6	7.7	4.4	2.2
sw (t2) (ppm)	66	5.5	35	66	38	40	35
Acq.time (t2) (ms)	16.4	3.8	9	6.6	8.7	9.1	9.1
sw (t3) (ppm)	100	100	100	100	100	40	35
Acq.time (t3) (ms)	8	8	8	8	8	9.1	8.8
sw (t4) (ppm)	–	–	-	–	-	100	30
Acq.time (t5) (ms)	–	–	-	–	-	8	8
^{1}H decoupling	swTPPM	swTPPM	swTPPM	swTPPM	swTPPM	waltz	swTPPM
Field (kHz)	26	26	26	26	26	7.2	13
Interscan delay (s)	1	0.8	0.8	1	0.8	1.25	1
Number of scans	8	80	240	8	16	48	16
NUS (%)	–	–	–	–	–	2	–
Measurement time (d)	3	2.4	11.5	3	4.6	5.5	13

Resonance Assignment. We used FLYA(8) (34) with peak lists generated from spectra of the fully-protonated sample automatically in Sparky(9) or CCPN (10)(36). The threshold for peak identification was initially set such that only an estimated 5-10 false peaks were present (as determined by the number of peaks picked with incorrect sign). Subsequently, overlapping peaks and weaker peaks (that were not initially picked) were manually identified to extend the assignment. The automated assignments were verified and additional assignments completed manually.

Structure Calculation. Several unambiguous distance restraints were manually assigned in the well resolved 3D (H)N(HH)NH spectrum for the solution sample. Similarly, the 4D (H)NH(H)NH spectrum was used to identify unambiguous restraints in the lipid bilayer sample. We additionally used the chemical shifts to generate dihedral angle restraints using TALOS-N(11). These initial unambiguous restraints and dihedral angles clearly defined the β-barrel region, and additional structure in the loops for the lipid bilayer preparation. For the solution structure, an initial set of hydrogen bond restraints was defined for resonances that showed no exchange in D_2O. For both structures, hydrogen bond restraints were included where cross-peaks in the 4D spectrum were identified (Fig S3-4), and where chemical shifts were consistent with an extended conformation, as indicated in Fig. S9. A short stretch of helical hydrogen bonds in loop 2 was introduced for the bilayer structure, where chemical shifts indicated, and where an initial model showed a helical structure (Fig. S9). NOESY peak lists (solution) or RFDR and BASS-SD peak lists (solids) were added for automated assignment and structure calculation using CYANA 3.98 (12). Final numbers are listed in Extended Data Table 2. Figures were prepared with UCSF Chimera (13).

Table S2: Structure calculation statistics. Summary of identified cross-peaks and conformational restraints used in the structure calculation, and structure quality in terms of RMSD within a bundle of 20 conformers used to represent the ensemble.

Distance restraints	Lipids (MAS)	Detergents (solution)
Total	769	112
Short-range (|i-j|<=1)	425	53
Medium-range (1<|i-j|<5)	21	3
Long-range (|i-j|>=5)	323	56
h-bonds (manual restraints)	94	64
Dihedral angle restraints	303	206
Restraints per residue ˜	3.1 (3.7*)	1.3 (2.8#)
Backbone RMSD (Å)	0.66*	0.73#
Heavy atom RMSD (Å)	1.40*	1.52#

*calculated over structured regions, residues 12-33, 44-108, 116-156, 161-205 (22+65+41+45=173 residues)
˜excluding short-range restraints, excluding H-bond restraints to avoid overcounting.
#calculated over structured regions, residues 13-27, 52-74, 100-107, 116-126, 146-169 ,193-205 (15+23+8+11+24+13=94 residues)

Table S3. Residue specific chemical shift perturbation (CSP) and amide ^{15}N relaxation.

Residue	Octane CSP (ppm)	Carvone CSP (ppm)	Apo ^{15}N R_1 (s^{-1})	Apo ^{15}N $R_{1\rho}$ (s^{-1})
12	0.050	0.024		
13	0.094	0.034		18.6 ±0.01
14	0.022	0.033	0.047 ±0.004	12.0 ±0.06
15	0.026	0.030		
16	0.035	0.036		
17	0.049	0.031		
18	0.034	0.082		
19	0.063	0.026	0.019 ±0.005	7.7 ±0.12

20	0.035	0.039		9.2 ±0.11
21	0.167	0.069		8.6 ±0.09
22	0.057	0.056	0.014 ±0.003	10.4 ±0.10
23	0.050	0.111	0.024 ±0.005	
–				
25	0.159	0.062		
26	0.268			
27	0.080			
28	0.078			
29				
30	0.097			
31	0.042	0.044	0.093 ±0.045	17.7 ±0.26
32	0.332		0.040 ±0.013	22.8 ±0.57
33	0.047			11.7 ±0.21
34	0.054			
–				
39	0.024			
40	0.142			
41	0.073			
–				
45		0.113		
46	0.018	0.032		14.3 ±0.16
47	0.030	0.036		
48	0.283	0.107		
49			0.043 ±0.010	16.3 ±0.21
–				
54	0.026	0.067		
55	0.072	0.094		16.3 ±0.30
56	0.091	0.113	0.019 ±0.003	
57	0.147	0.082	0.024 ±0.006	9.4 ±0.11
58	0.133	0.096		
59	0.098	0.049	0.015 ±0.002	
60	0.055	0.035	0.014 ±0.004	10.3 ±0.13
61	0.055	0.018		5.9 ±0.06
62	0.020	0.033	0.013 ±0.003	7.8 ±0.06
63	0.046	0.051	0.025 ±0.006	15.0 ±0.25
64	0.032	0.053		
65	0.034	0.045		
66	0.027	0.040		108.4 ±3.8
67	0.024	0.010		11.5 ±0.09
68	0.030	0.032	0.013 ±0.002	7.7 ±0.04
69	0.020	0.025	0.012 ±0.002	5.8 ±0.03
70	0.035	0.023	0.014 ±0.002	7.3 ±0.04
71	0.066	0.031		
72	0.119	0.090	0.010 ±0.003	8.0 ±0.06
73	0.045			
–				
75			0.028 ±0.009	12.0 ±0.14
–				
77	0.365	0.188		28.0 ±0.67
78	0.121			
79	0.168	0.372	0.040 ±0.009	14.6 ±0.18
80	0.101	0.230		
81	0.169	0.025		13.2 ±0.18
82	0.154	0.166		

83	0.084	0.049	0.023 ±0.004	
84	0.054	0.018		12.4 ±0.07
85	0.029	0.041	0.037 ±0.004	12.8 ±0.08
86	0.099	0.062		
87	0.060	0.039		
88	0.150	0.049	0.091 ±0.029	13.4 ±0.21
89	0.087	0.055	0.040 ±0.010	13.5 ±0.16
90	0.124	0.068		
91	0.082	0.071	0.074 ±0.011	11.6 ±0.09
92	0.028	0.038	0.052 ±0.005	10.9 ±0.06
93	0.047	0.041	0.029 ±0.005	7.8 ±0.08
94	0.026	0.059	0.017 ±0.002	6.4 ±0.04
95	0.060	0.043		
96	0.094	0.099		9.5 ±0.07
97				12.6 ±0.26
–				
99	0.339	0.066	0.047 ±0.013	14.0 ±0.27
–				
101			0.029 ±0.008	
102	0.091	0.099	0.014 ±0.004	7.9 ±0.07
103	0.087	0.068	0.008 ±0.002	5.5 ±0.04
104	0.030	0.020	0.014 ±0.002	10.1 ±0.06
105	0.026	0.044	0.013 ±0.002	
106	0.056	0.057		
107	0.027	0.042	0.010 ±0.002	6.2 ±0.04
108	0.004	0.044		
109	0.123	0.078	0.006 ±0.002	9.6 ±0.07
110		0.041		
–				
115	0.148			
116	0.062			
–				
118	0.077	0.011		
119	0.036	0.029		
120	0.059	0.027	0.019 ±0.003	9.6 ±0.08
121	0.015	0.022	0.013 ±0.004	9.0 ±0.08
122	0.030	0.055		
123	0.044	0.045	0.018 ±0.004	5.7 ±0.05
124	0.101	0.123	0.018 ±0.004	10.8 ±0.11
125	0.129	0.087		9.9 ±0.12
126	0.337	0.170		
127	0.256	0.176	0.016 ±0.007	
128	0.022			
129	0.021			
130	0.031	0.051	0.034 ±0.006	
131	0.066	0.135		
132	0.082	0.072	0.028 ±0.004	7.7 ±0.08
133	0.014	0.022		
134	0.029	0.054	0.030 ±0.005	11.4 ±0.08
135	0.135	0.046	0.030 ±0.006	6.6 ±0.07
136	0.046	0.051		
137	0.067	0.037		
138	0.052	0.035	0.016 ±0.003	15.2 ±0.12
139	0.028	0.017		15.5 ±0.10
140	0.029	0.015		

141	0.097	0.063		6.0 ±0.06
142	0.223	0.206	0.041 ±0.009	8.7 ±0.01
143	0.028	0.022	0.045 ±0.005	7.7 ±0.04
144	0.133	0.050		9.4 ±0.12
145	0.133	0.104		9.3 ±0.21
146	0.064	0.111		9.8 ±0.12
–				
148	0.057	0.017		8.3 ±0.06
149	0.044	0.065		
150	0.043	0.030	0.009 ±0.002	9.1 ±0.05
151	0.012	0.031	0.011 ±0.002	7.9 ±0.04
152	0.035	0.060		
153	0.022	0.043	0.022 ±0.003	7.7 ±0.05
154	0.031	0.051		
155	0.022	0.024		
156	0.054	0.040		
157	0.049			
158	0.033			
–				
161	0.176	0.102		
162	0.012	0.033	0.025 ±0.008	10.4 ±0.11
163	0.031	0.034		
164	0.026	0.027		
165	0.035	0.040	0.029 ±0.003	6.6 ±0.04
166	0.048	0.028	0.027 ±0.006	9.3 ±0.09
167	0.069	0.071	0.014 ±0.002	7.1 ±0.04
168	0.069	0.115		
169	0.107	0.070		
–				
172	0.348	0.283		
173	0.264	0.204		
174	0.034		0.053 ±0.007	10.5 ±0.01
175	0.144	0.055	0.090 ±0.015	8.9 ±0.07
176	0.057	0.017		
177	0.039	0.033		
178	0.019	0.032	0.018 ±0.002	6.8 ±0.04
179	0.065	0.034	0.026 ±0.003	8.0 ±0.05
180	0.212	0.042		
181	0.182	0.035		
–				
183	0.003	0.017		
–				
185	0.044	0.020		
186	0.086	0.027		
187	0.205	0.105	0.040 ±0.009	11.1 ±0.15
188	0.112	0.066		13.0 ±0.18
189	0.057	0.053		
190	0.053	0.022		
191	0.156			14.7 ±0.17
–				
194	0.352			
195	0.224	0.123		
196	0.033	0.008	0.014 ±0.002	6.1 ±0.06
197	0.152	0.129	0.021 ±0.005	11.0 ±0.23
198	0.031	0.055		

199	0.031	0.019	0.010 ±0.003	9.0 ±0.07
200	0.070	0.037	0.016 ±0.004	7.2 ±0.07
201	0.059	0.028	0.016 ±0.005	8.3 ±0.09
202	0.041	0.066	0.019 ±0.004	9.6 ±0.09
203	0.045			
204	0.098			

***Relaxation data fitting*.** Signal intensity decays of both ^{15}N R_1 and $R_{1\rho}$ relaxation experiments were fitted to a monoexponential function. Error estimate was performed with Monte Carlo simulations: synthetic datasets are produced by adding Gaussian random noise (with same standard deviation as the experimental noise) to the back-calculated decay curves. The error was determined as the standard deviation of the ensemble of dynamical parameters obtained by fitting 1000 synthetic datasets.

MD Simulations: System preparation - AlkL NMR structure. The NMR structure of AlkL was aligned along the membrane normal using the Orientations of Proteins in Membranes (OPM) database(14) and subsequently embedded in a DMPC or LPS membrane and solvated with water molecules and 150 mM KCl using the CHARMM-GUI webserver (15). The full system contained ~160 000 atoms. The titratable groups of the protein were protonated according to their standard protonation states at pH 7, with an exception of D58, which was protonated, based on the spatial proximity of another negatively charged residue, D70 and robust binding of K^+ ion to (charged) D58 in initial simulations. Further, pKa values predicted by PROPKA(16) suggested that one of these aspartates (D58 or D70) should be in its protonated form.
The initial, multi-step equilibration of the system, with a gradual release of restrains acting on protein atoms, was conducted using scripts provided by CHARMM-GUI. Subsequently, the system was equilibrated for 100 ns, without any restraints, prior to production runs.
To study interactions and possible permeation of hydrophobic molecules through AlkL, 64 carvone molecules were placed in the aqueous phase of the last snapshot from the equilibration run.

***MD Simulations: System preparation - AlkL homology models*.** Two homology models of AlkL were built, using structures of OmpW and OprG proteins (PDB id: 2F1T and 2X27, respectively) as templates using the Swiss-model web server (swissmodel.expasy.org). Both homology models were then prepared for MD simulations in the same manner as the NMR structure.

***MD Simulation details*.** All simulations were performed with GROMACS 2018 simulation software(17). The CHARMM36m force field was used in all simulations (18). Lipids were modeled using the CHARMM36 force field (19). The *P. Aruginosa* LPS was chosen with Lipid A type 1, core 2, and 2x the standard O-antigen in the CHARMM gui (www.charmm-gui.org) with calcium counterions. The parameters for carvone were obtained from the CHARMM General Force Field (CGenFF) (20) webserver (https://cgenff.paramchem.org). Water was modeled using the CHARMM version of the TIP3P model(21), with LJ interactions placed on hydrogen atoms. Standard CHARMM parameters were used for K^+, Ca^{2+} and Cl^- ions (22). All bonds were constrained using LINCS, allowing for a 2fs time step (23). Non-bonded (van der Waals) interactions were force-switched off from 0.8 to 1.2 nm. Long-range electrostatic interactions were treated with PME with a 1.2 nm real space cutoff (24). The simulated systems were kept at a temperature of 320K and a pressure of 1 bar, using a Nosé-Hoover thermostat (25, 26) and a Parrinello-Rahman barostat(27), respectively.
For LPS simulations (Fig. S6), an initial simulation was carried out for 100 ns and 10 equidistant frames from this trajectory were extracted. Into each of these 10 frames, 100 randomly placed octanes were inserted, replacing about 1000 water molecules. Each of these 10 octane-containing frames were independently equilibrated 10 times and the 100 simulations were run for a total of ~15 μs. The top 10 trajectories (defined by the octane with the most contacts with AlkL and manually verified to be close to the exit site) out of these initial 100 were chosen and another 10 replicas from each were spawned and run for a total of ~50 μs.
The simplified DMPC-octane simulations were run in the presence of 64 randomly placed octanes in 11 independent simulations for a total of ~9 μs (Fig. S6).
Four systems containing AlkL in DMPC were simulated for 1000 ns each ('Alk apo' simulations). After the addition of carvone, four new systems were initially simulated for 1000 ns each. Further simulations were spawned by monitoring the position of bound carvone and simulated for additional 100 ns in several cycles, as shown in Fig. S7.

Systems containing homology models of AlkL were simulated with and without carvone for 1000 ns in 4 copies each. The total simulation time of all systems was ~34 μs and for the entire study, about 108 μs.

MD Simulation analysis. Exit pathways were identified and analysed using the MOLE 2.0 software(28) and CONAN (29). Remaining analysis was performed using GROMACS tools: cluster, covar, anaeig, distance and in-house written scripts. Molecular structures were rendered using VMD (30). Plots were made using NumPy and Matplotlib.

Supporting Figures

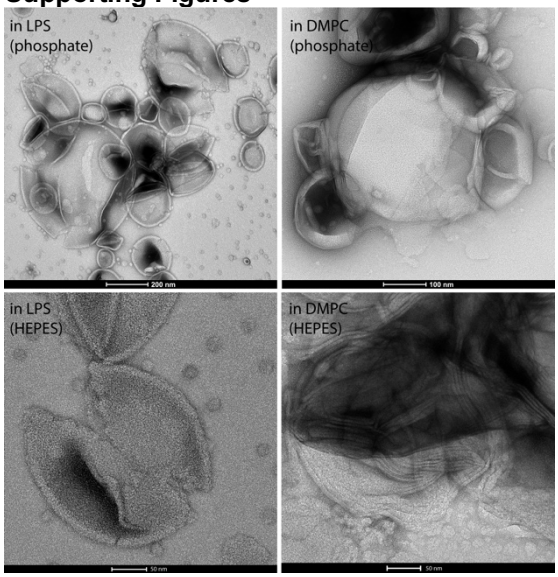

Figure S1. Negative stain EM images of the preparations used for NMR. Liposomes are observed. No protein aggregate was identified, and no evidence for ordered 2D crystalline arrays could be found.

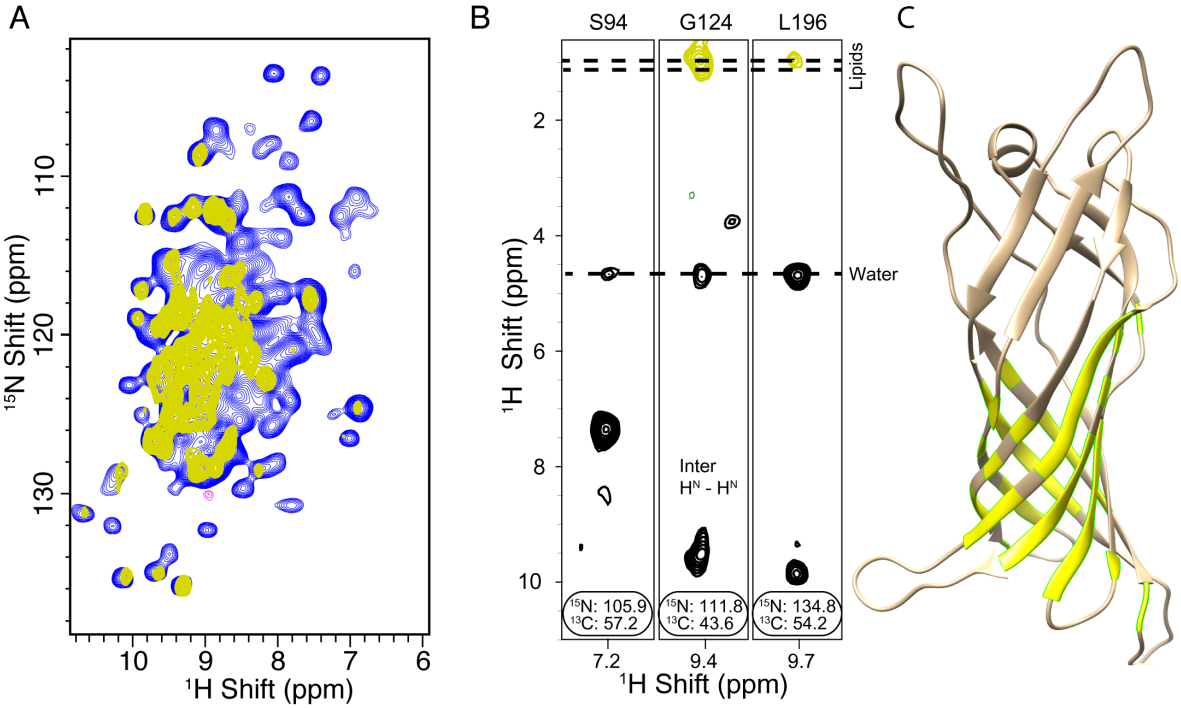

Figure S2. Lipid to protein magnetization transfer shows the lipid-embedded protein surface. In (A), the lipid plane of a 3D HhNH spectrum at about 1.1 ppm is colored in yellow. In (B) selected strips from a similar 4D spectrum, HhnCANH resolves resonance overlap in the 3D spectrum. 50 ms of Nuclear Overhauser Effect (NOE) mixing was used. In C, the residues for which lipid contacts are observed are colored in yellow on the solid-state NMR structure. Spectra were acquired at a 800 MHz spectrometer with 55 kHz MAS. The protein was deuterated to suppress any protein signals arising at the proton frequency of the lipid acyl chains.

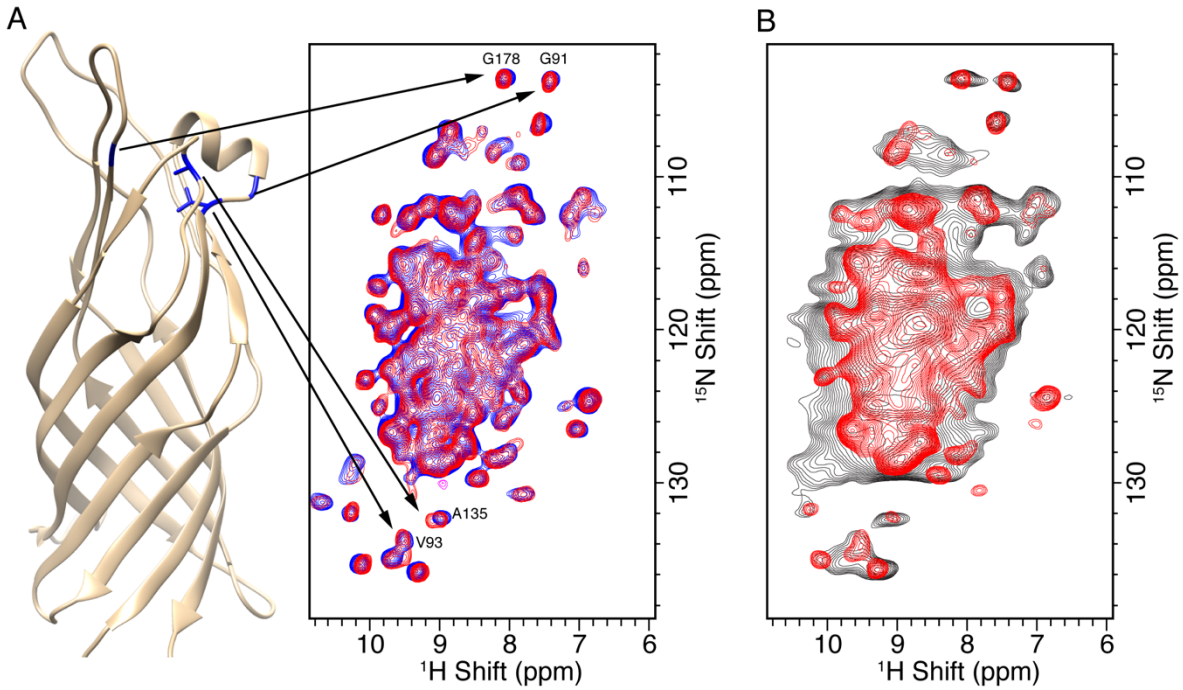

Figure S3. Spectra at varying DMPC lipid concentration. In (A), the a lipid protein ratio (LPR) of 10 (blue) is compared with a LPR of 0.5 (red). The spectra are nearly identical, and notably, several well-resolved resonances from the loops are unchanged in the dilute sample. In (B), degradation of the spectral quality is observed for an over concentrated sample with LPR of 0.25 (black) compared with a sample at 0.5 LPR (red). All spectra were recorded on a 700 MHz spectrometer with a spinning frequency of 60 kHz. Spectra in (A) were recorded with deuterated protein, and those in (B) with protonated protein.

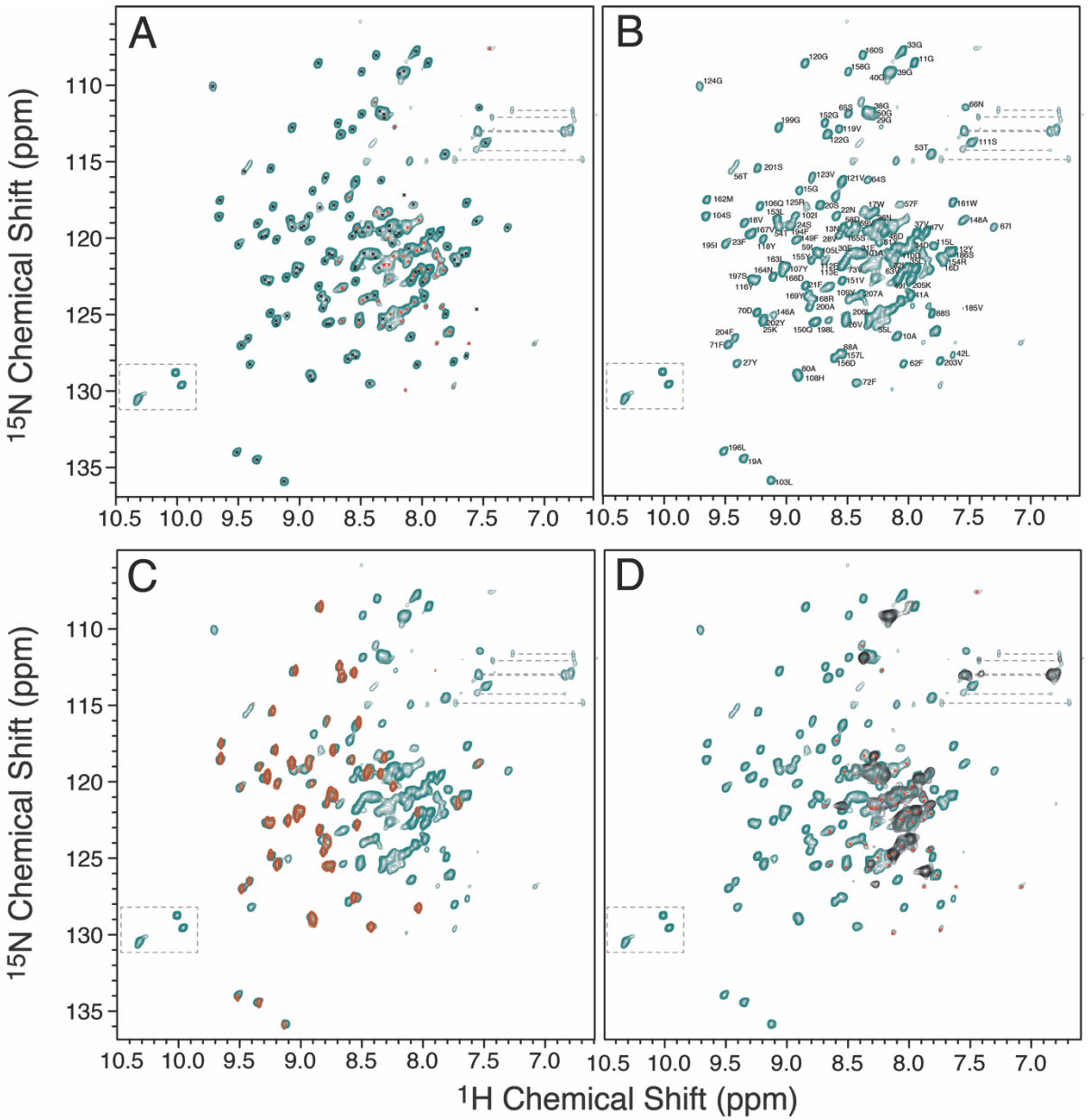

Figure S4. Solution ^{15}N-TROSY spectra of AlkL. In (A and D), unassigned resonances are indicated with red crosses. In (B), assignments are annotated. In (C), the red spectrum was recorded after 24 hours in D_2O, indicating exceptionally stable hydrogen bonds, which were used in the structure calculation. In (D), the black spectrum was recorded on AlkL in MSP1D1 DMPC nanodiscs. Only signals arising from highly flexible loops are detected, prohibiting structural analysis under these conditions. Notably, many signals that were flexible and unassigned in (A) are not detected. This data is consistent with the MAS NMR spectra in which we were not able to assign 18 N- and C- terminal residues, as well as part of L1, T2 and T3, and the His_8 tag. The absence of peaks in assignment spectra indicates that some of these unassigned resonances correspond to residues that are highly flexible.

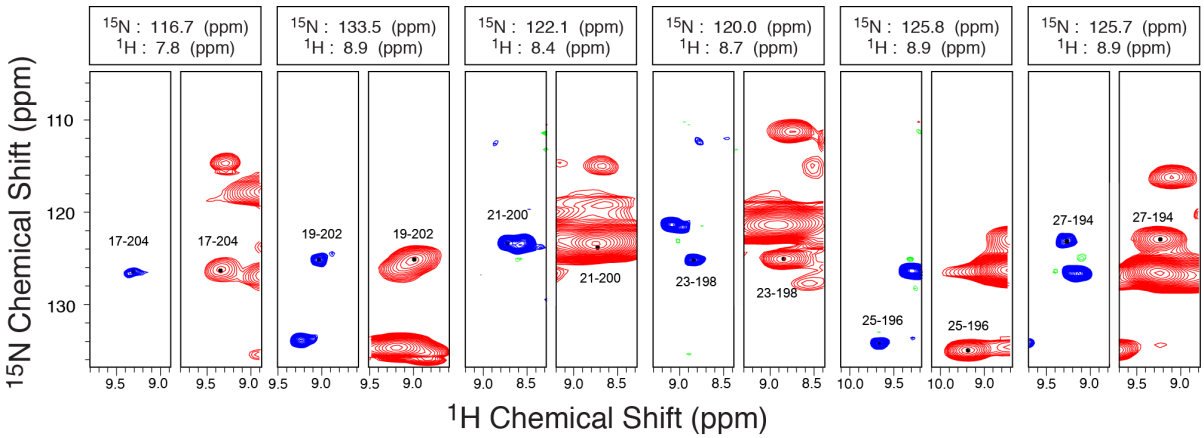

Figure S5. Inter-proton proximities. Selected planes from two 4D (H)NH(H)NH spectra (using RFDR for proton-proton mixing). In blue, the spectrum was recorded with high resolution, but lower sensitivity, by sampling the proton dimension to 4 ms. In red, the spectrum was recorded with shorter indirect proton evolution of 2 ms which resulted in higher sensitivity, but lower resolution. The first 2 planes (connecting residues 17-204) show an example where the peak was just above noise in the blue spectrum, and clearly found in the red spectrum. The third 2 planes (connecting residues 21-200) shows an example where the longer evolution times in the blue spectrum was necessary, and the peak is indistinguishable from the diagonal in the red spectrum. Both spectra were used in conjunction to construct a consistent set of nearly unambiguous contacts, and to build the initial model (see Fig. S6).

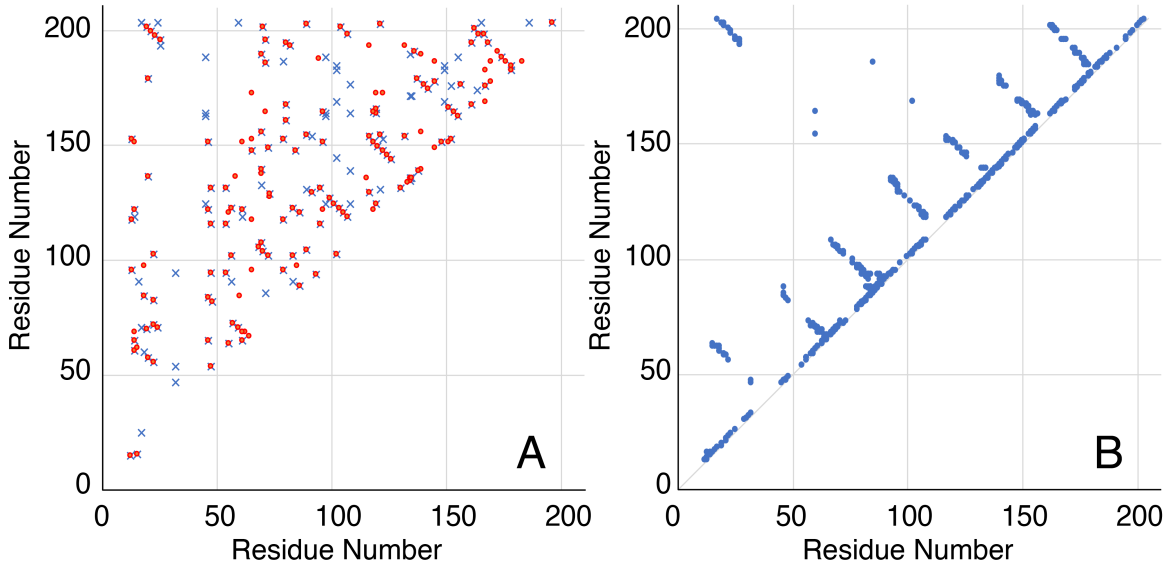

Figure S6. Proton-proton contact maps. In (A), automatically generated contacts from peaks picked from the (H)NH(H)NH spectra of Fig. S5. A threshold of 0.5 ppm (^{15}N) and 0.11 ppm (^{1}H) were used to generate all possible assignments. Contacts arising from one side of the spectrum's diagonal are shown in red, while those from the other are shown in blue. A clear pattern of antiparallel β-strands emerges, despite some degeneracy in the ^{1}H-^{15}N plane used to identify starting and ending signal. In (B), the contact map of the final structure is shown, after resolution of ambiguities using CYANA, and including contacts from all spectra. The additional restraint assignment possibilities in (A) arising from degenerate chemical shifts have been removed in (B).

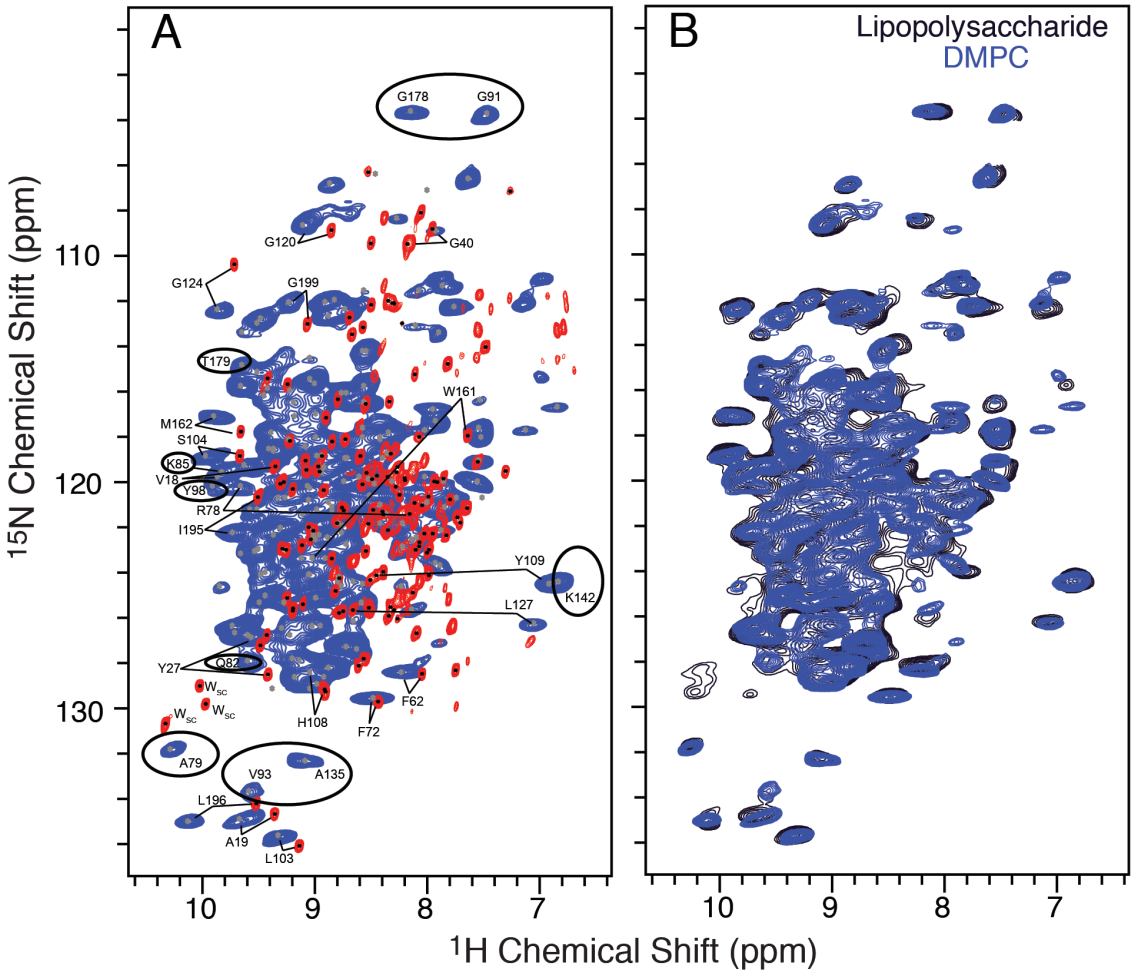

Figure S7. Solution and solid-state NMR spectra of AlkL. In A, the solution ^{15}N-^{1}H HSQC spectrum (red) is compared with the dipolar ^{15}N-^{1}H correlation acquired on the DMPC lipid bilayer sample (blue). Residues that were assigned in lipids, but could not be assigned in solution are encircled. Some of the residues outside the TM region displayed large differences in chemical shift, such as R78, Y109, L127, and W161, indicating the change from ordered to disordered. The remaining unassigned amide proton shifts in solution fall between 7.5 and 8.7 ppm, indicating a lack of β-sheet secondary structure. In B, the DMPC sample (blue) is compared with a sample reconstituted in 50% lipopolysaccharide (LPS) with a ratio of 1:0.5:0.5 AlkL:DMPC:LPS (w/w/w) (black). The spectra were contoured from 25% of the intensity of the G178 peak. The spectrum obtained in LPS, with only minor chemical shift changes, indicates that the structured extracellular loops are stable in the near native environment including lipopolysaccharides that are typically found on the outside of the asymmetric bacterial outer membrane. In the reconstituted sample, neither the AlkL, nor the LPS are oriented.

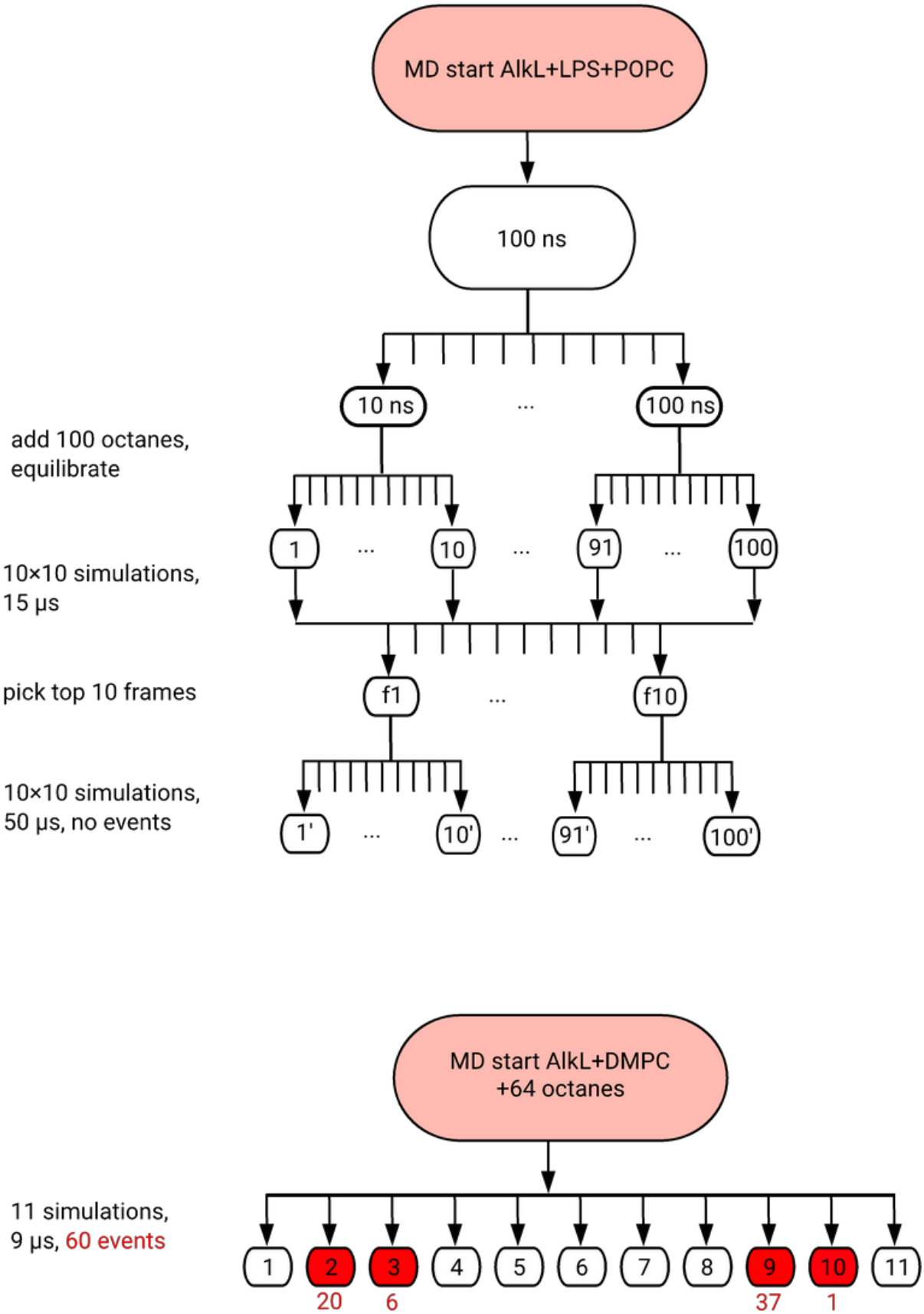

Figure S8. Simulation protocol for octane permeation through AlkL. Single numbers label individual simulation replicas. Simulations in which an octane molecule spontaneously permeated through the protein are indicated in red, along with the number of transit events observed.

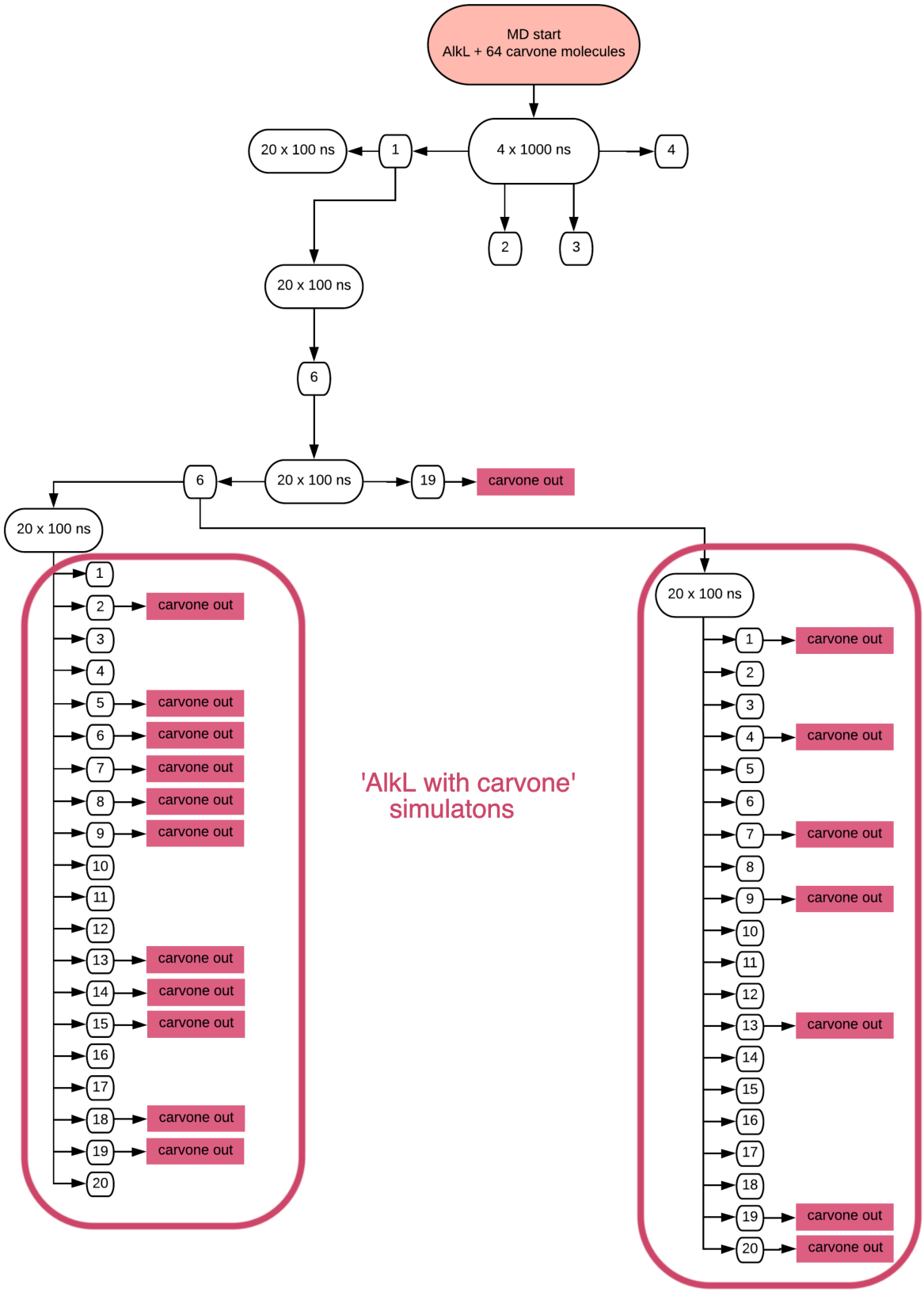

Figure S9. Simulation protocol for carvone permeation through AlkL. Single numbers label individual simulation replicas. Simulations in which a carvone molecule spontaneously permeated through the protein are labelled with boxes 'carvone out'. The 40 simulations referred to as 'AlkL with carvone' in the main text are enclosed within the rounded maroon boxes.

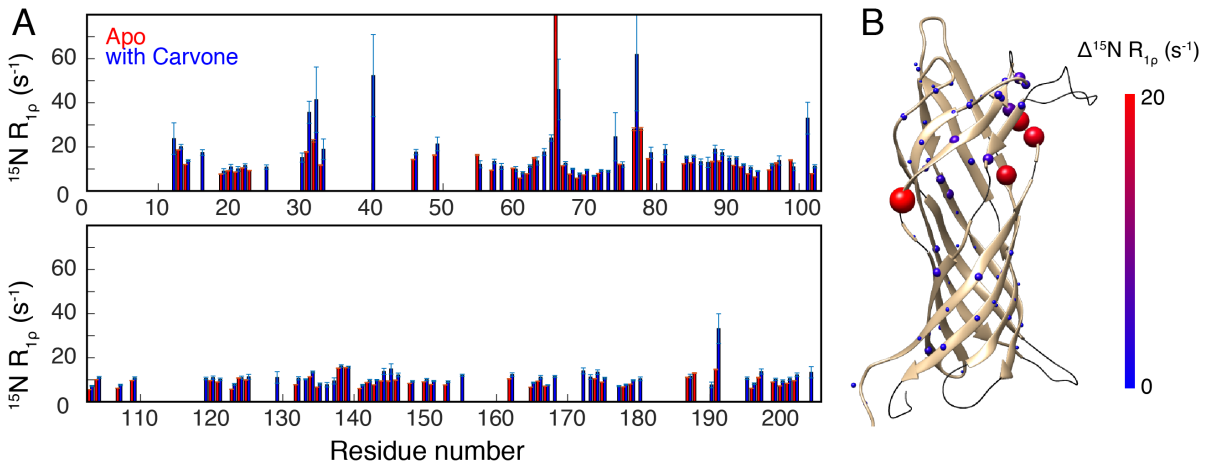

Figure S10. Dynamic parameter perturbations highlight weak binding sites of carvone. In A, transverse relaxation rates are shown for apo (red) and carvone saturated (blue) samples, as determined from (H)CONH spectra. In B, the difference in rates is shown on the structure.

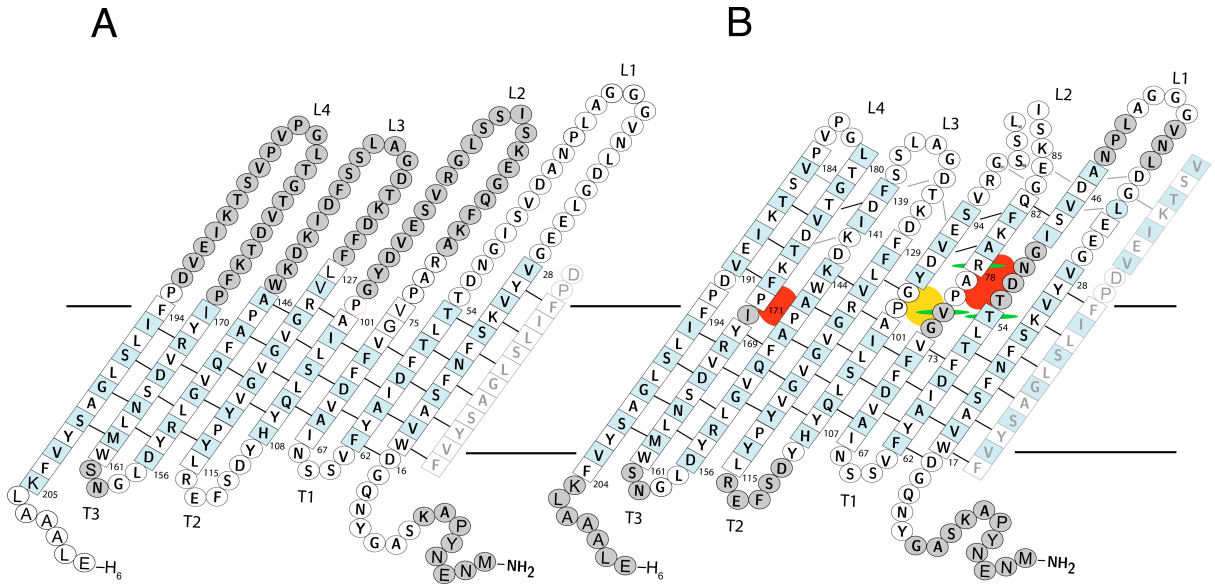

Figure S11. Topology map of AlkL as determined by NMR, both in detergent micelles (A) and in lipid bilayers (B). Assigned residues with chemical shifts consistent with β-sheet conformation are indicated in boxes, while other assigned residues are indicated with white circles. Unassigned residues are in grey circles. Blue residues point toward the interior. In lipids, a hydrophobic volume is formed in the extracellular barrel extension. The interior of the transmembrane β-barrel is packed densely with the side-chains of charged residues, while hydrophobic residues point out, as expected. Intracellular turns are numbered as T1-T3, and extracellular loops are numbered L1-L4. In both panels, in order to render the circular barrel topology, the last β-strand is repeated on the right-hand side and grayed out. The approximate position of the membrane is indicated by horizontal lines. The new and previous proposed exit sites are shown as red and yellow ovals, respectively, and packing interactions in OmpW crystals are indicated by green lines.

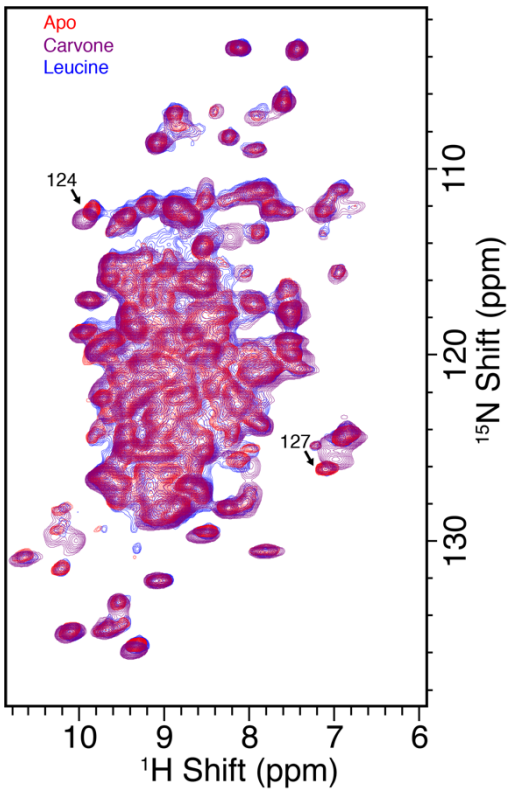

Figure S12. Chemical shift perturbations due to saturation with carvone (purple), which has about 7-8 mM solubility in water(31) and 1 mg/ml (8 mM) Leucine (blue). Shift changes of similar magnitude are observed with octane, which has a very low solubility in water (only about 60 nM according to the CDC NIOSH https://www.cdc.gov/niosh/npg/npgd0470.html. The shift changes due to carvone are evident in the 2D spectrum. For leucine, no shift changes are seen, consistent with the expectation that AlkL does not act as a channel for amino acids.

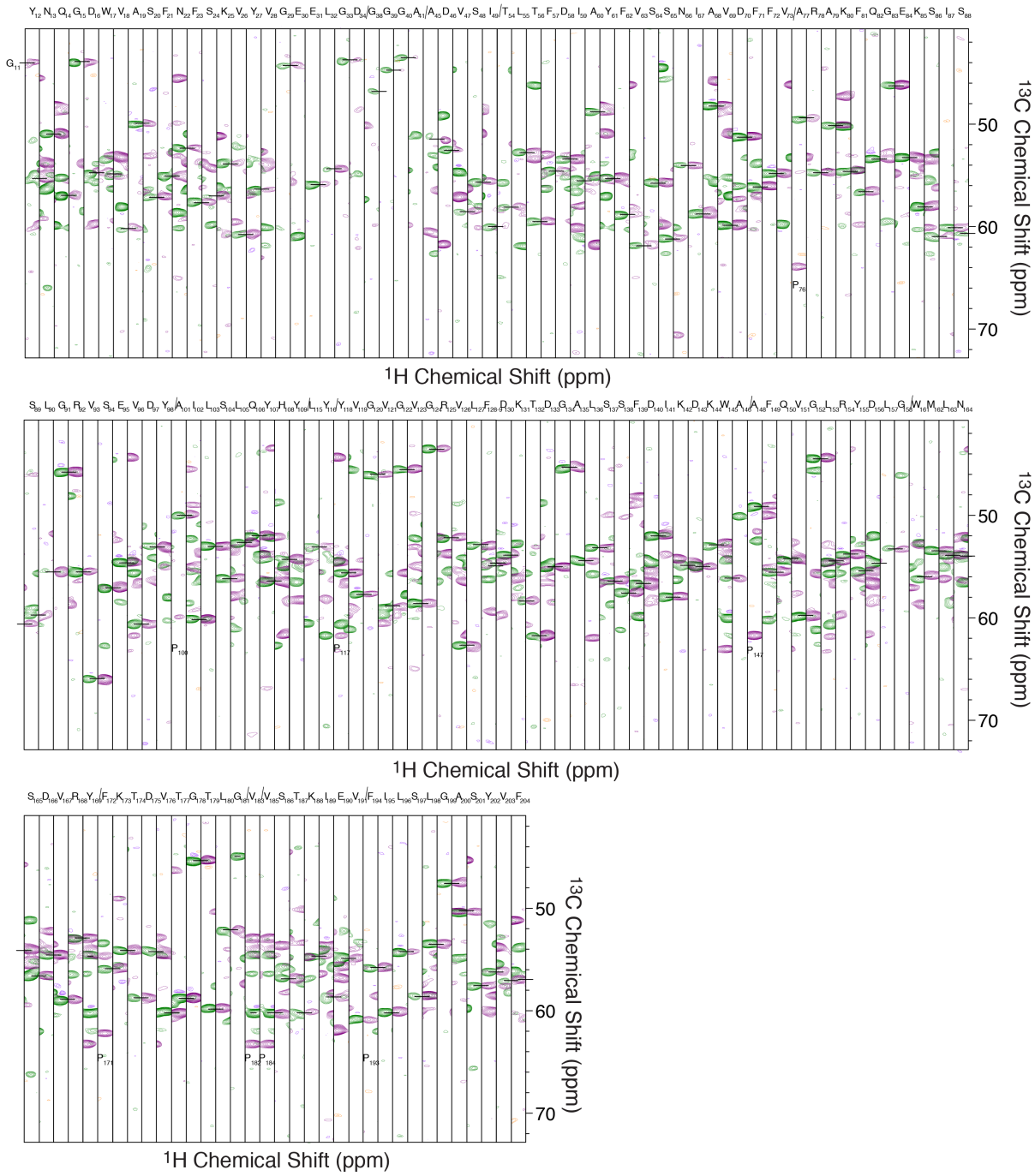

Figure S13. Backbone resonance assignment. Linking of sequential NH moieties in the (H)CANH (green) and (H)(CO)CA(CO)NH (purple) spectra of ^{2}H,^{13}C,^{15}N AlkL in lipid bilayers. Strips corresponding to each assigned NH group are shown. The sequence specific assignment is indicated above each strip, and a slash indicates where assignments are missing.

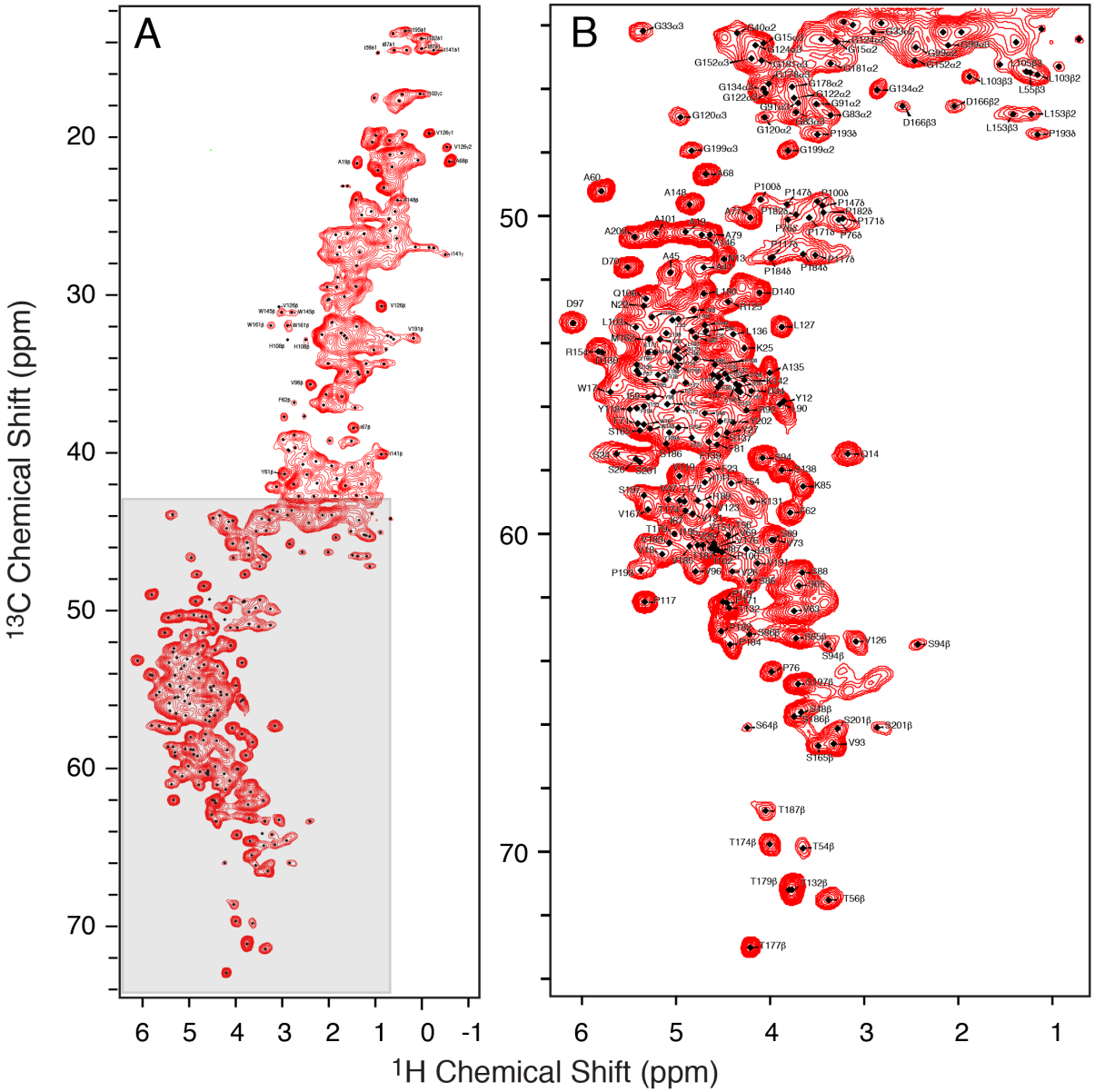

Figure S14. Solid-state NMR ^{1}H-^{13}C dipolar correlation spectrum recorded on lipid bilayer embedded U-^{13}C,^{15}N AlkL using 111 kHz magic-angle spinning. Assignments are shown for the C□-H□ region (right), as well as for selected isolated side-chain peaks (left).

SI Movie. The motion along the first (largest) eigenvector in a principal component analysis of MD snapshots with and without the molecule carvone. The motion shows that the difference without and with bound carvone is related to the opening of the newly identified site I for carvone permeation.

SI References

1. Schwarzer TS, Hermann M, Krishnan S, Simmel FC, & Castiglione K (2017) Preparative refolding of small monomeric outer membrane proteins. *Protein Expr. Purif.* 132:171-181.
2. Jain MG*, et al.* (2017) Selective (1)H-(1)H Distance Restraints in Fully Protonated Proteins by Very Fast Magic-Angle Spinning Solid-State NMR. *J. Phys. Chem. Lett.* 8:2399-2405.
3. Ritchie TK*, et al.* (2009) Chapter 11 - Reconstitution of membrane proteins in phospholipid bilayer nanodiscs. *Methods Enzymol.* 464:211-231.
4. Salzmann M, Wider G, Pervushin K, Senn H, & Wuthrich K (1999) TROSY-type triple-resonance experiments for sequential NMR assignments of large proteins. *J. Am. Chem. Soc.* 121:844-848.
5. Barbet-Massin E*, et al.* (2014) Rapid proton-detected NMR assignment for proteins with fast magic angle spinning. *J. Am. Chem. Soc.* 136:12489-12497.
6. Stanek J*, et al.* (2016) NMR Spectroscopic Assignment of Backbone and Side-Chain Protons in Fully Protonated Proteins: Microcrystals, Sedimented Assemblies, and Amyloid Fibrils. *Angew. Chem. Int. Ed. Engl.* 55:15504-15509.
7. Bennett AE, Ok JH, Griffin RG, & Vega S (1992) Chemical-Shift Correlation Spectroscopy in Rotating Solids - Radio Frequency-Driven Dipolar Recoupling and Longitudinal Exchange. *J. Chem. Phys.* 96:8624-8627.
8. Schmidt E & Guntert P (2012) A new algorithm for reliable and general NMR resonance assignment. *J. Am. Chem. Soc.* 134:12817-12829.
9. Lee W, Tonelli M, & Markley JL (2015) NMRFAM-SPARKY: enhanced software for biomolecular NMR spectroscopy. *Bioinformatics* 31:1325-1327.
10. Vranken WF*, et al.* (2005) The CCPN data model for NMR spectroscopy: development of a software pipeline. *Proteins* 59:687-696.
11. Shen Y & Bax A (2013) Protein backbone and sidechain torsion angles predicted from NMR chemical shifts using artificial neural networks. *J. Biomol. NMR* 56:227-241.
12. Güntert P & Buchner L (2015) Combined automated NOE assignment and structure calculation with CYANA. *J. Biomol. NMR* 62:453-471.
13. Pettersen EF*, et al.* (2004) UCSF Chimera--a visualization system for exploratory research and analysis. *J. Comput. Chem.* 25:1605-1612.
14. Lomize MA, Pogozheva ID, Joo H, Mosberg HI, & Lomize AL (2012) OPM database and PPM web server: resources for positioning of proteins in membranes. *Nucleic Acids Res.* 40:D370-376.
15. Jo S, Kim T, Iyer VG, & Im W (2008) CHARMM-GUI: a web-based graphical user interface for CHARMM. *J. Comput. Chem.* 29:1859-1865.
16. Olsson MH, Sondergaard CR, Rostkowski M, & Jensen JH (2011) PROPKA3: Consistent Treatment of Internal and Surface Residues in Empirical pKa Predictions. *J. Chem. Theory Comput.* 7:525-537.
17. Van Der Spoel D*, et al.* (2005) GROMACS: fast, flexible, and free. *J. Comput. Chem.* 26:1701-1718.
18. Huang J*, et al.* (2017) CHARMM36m: an improved force field for folded and intrinsically disordered proteins. *Nat. Methods* 14:71-73.
19. Klauda JB*, et al.* (2010) Update of the CHARMM all-atom additive force field for lipids: validation on six lipid types. *J Phys Chem B* 114:7830-7843.
20. Vanommeslaeghe K*, et al.* (2010) CHARMM general force field: A force field for drug-like molecules compatible with the CHARMM all-atom additive biological force fields. *J. Comput. Chem.* 31:671-690.
21. MacKerell AD*, et al.* (1998) All-atom empirical potential for molecular modeling and dynamics studies of proteins. *J. Phys. Chem. B* 102:3586-3616.
22. Beglov D & Roux B (1994) Finite Representation of an Infinite Bulk System - Solvent Boundary Potential for Computer-Simulations. *J. Chem. Phys.* 100:9050-9063.
23. Hess B, Bekker H, Berendsen HJC, & Fraaije JGEM (1997) LINCS: A linear constraint solver for molecular simulations. *J. Comput. Chem.* 18:1463-1472.
24. Darden T, York D, & Pedersen L (1993) Particle Mesh Ewald - an N.Log(N) Method for Ewald Sums in Large Systems. *J. Chem. Phys.* 98:10089-10092.
25. Hoover WG (1985) Canonical dynamics: Equilibrium phase-space distributions. *Phys. Rev. A Gen. Phys.* 31:1695-1697.

26. Nose S (1984) A Unified Formulation of the Constant Temperature Molecular-Dynamics Methods. *J. Chem. Phys.* 81:511-519.
27. Parrinello M & Rahman A (1981) Polymorphic Transitions in Single-Crystals - a New Molecular-Dynamics Method. *J. Appl. Phys.* 52:7182-7190.
28. Sehnal D*, et al.* (2013) MOLE 2.0: advanced approach for analysis of biomacromolecular channels. *J. Cheminform.* 5:39.
29. Mercadante D, Grater F, & Daday C (2018) CONAN: A Tool to Decode Dynamical Information from Molecular Interaction Maps. *Biophys. J.* 114:1267-1273.
30. Humphrey W, Dalke A, & Schulten K (1996) VMD: visual molecular dynamics. *J. Mol. Graph.* 14:33-38, 27-38.
31. Fichan I, Larroche C, & Gros JB (1999) Water solubility, vapor pressure, and activity coefficients of terpenes and terpenoids. *J. Chem. Eng. Data* 44:56-62.